

RAWild: Sensor-Agnostic RAW Object Detection via Physics-Guided Curve and Grid Modeling

Shuhong Liu^{1,2,♣}, Gengjia Chang^{2,♣}, Jun Liu², Xuangeng Chu^{1,2}
Yinqiang Zheng¹, Tatsuya Harada^{1,3}, Ziteng Cui^{1,2,◇}

¹The University of Tokyo ²I2WM ³RIKEN



Figure 1: RAW object detection across sensors. Four benchmarks [Omid-Zohoor et al. \[2017\]](#), [Hong et al. \[2021\]](#), [Li et al. \[2025b\]](#), [Xu et al. \[2023\]](#) captured by distinct sensors under different environments, exposure settings, spectral sensitivities, and bit-depths exhibit substantially different pixel distributions, posing a fundamental challenge for sensor-agnostic generalization.

Abstract

Camera sensor RAW data offers intrinsic advantages for object detection, including deeper bit depth, preserved physical information, and freedom from image signal processor (ISP) distortions. However, varying exposure conditions, spectral sensitivities, and bit depths across devices introduce substantially larger domain gaps than sRGB, making sensor-agnostic generalization a fundamental challenge. In this study, we present **RAWild**, a physics-guided global-local tone mapping framework for sensor-agnostic RAW object detection. By factoring sensor-induced variations into a global tonal correction and a spatially adaptive local color adjustment, both driven by RAW distribution priors, our framework enables a single network to train jointly across heterogeneous sensors. To further support cross-sensor generalization, we construct a physics-based RAW simulation pipeline that synthesizes realistic sensor outputs spanning diverse spectral sensitivities, illuminants, and sensor non-idealities. Extensive experiments across multiple RAW benchmarks covering bit depths from 10 to 24 demonstrate state-of-the-art (SOTA) performance under single-dataset, mixed-dataset, and challenging robustness settings.

♣These authors contribute equally to this work. ◇Corresponding author.

SOTA performance not only on multiple established RAW benchmark datasets but also under mixed-dataset training regimes spanning heterogeneous sensors and bit-depths, as well as more challenging robustness scenarios involving severe degradation and domain shift, as illustrated in Figure 2.

Our key contributions could be summarized as follows:

- We propose **RAWild**, a histogram-guided global-local tone mapping framework for sensor-agnostic RAW object detection. It decomposes sensor variations into a global Bézier curve for tonal correction and a spatially-adaptive Bilateral Grid for local color refinement.
- We reparametrize both components with a delta-residual Bézier curve, and a gain-mixing decomposition of the Bilateral Grid that separates per-channel gain from color mixing, enabling stable training across heterogeneous RAW images.
- Extensive experiments on six per-sensor and mixed-sensor real-capture RAW benchmarks and three datasets synthesized by our physics-based RAW simulation pipeline, spanning 10- to 24-bit sensors, demonstrate consistent SOTA performance.

2 Related Work

Camera RAW-based Object Detection. RAW data preserves linear photon measurements with high dynamic range and avoids the irreversible loss of ISP Karaimer and Brown [2016], Delbracio et al. [2021], benefiting perception in low light Hong et al. [2021], Chen et al. [2018], Jiang et al. [2025] and HDR scene reconstruction Mildenhall et al. [2022], Jin et al. [2024], Li et al. [2024c], Kee et al. [2025]. Detection-oriented efforts either jointly learn task-aware ISPs with the detector Yu et al. [2021], Wang et al. [2024d], Li et al. [2024a], Kim et al. [2023], adapt sRGB-pretrained models to RAW with adaptive modules Cui and Harada [2024], Huang et al. [2025], or build RAW-native detectors spanning embedded Omid-Zohoor et al. [2017], low-light Guo et al. [2025], and diverse-condition settings Xu et al. [2023], Gamrian et al. [2025], Xie et al. [2026], Li et al. [2024b, 2025b,a]. These detectors remain optimized per sensor and are brittle to cross-sensor radiometric shifts.

Image Signal Processing with Bilateral Grid. Bilateral Grid Chen et al. [2007, 2016] embeds pixels in a 3D spatial-intensity space for efficient edge-aware operations sliced back to full resolution; HDRnet Gharbi et al. [2017] first paired it with deep learning to predict spatially-varying color transforms, joining other learned ISP components Gharbi et al. [2016], Heide et al. [2014]. Follow-ups cascade grids with neural 3D LUTs for retouching Kim and Cho [2024], Conde et al. [2024], Zehtab et al. [2025], embed per-view grids in radiance fields to disentangle ISP effects Wang et al. [2024b, 2025], or combine them with learned tonal curves and color-name priors Serrano-Lozano et al. [2024], Liu et al. [2024], Le et al. [2023]. We are the first to apply Bilateral Grids to RAW detection and couple them with a global Bézier curve to achieve physics-aware tonal mapping.

Sensor-Agnostic Computer Vision. Sensor-agnostic learning unifies heterogeneous inputs so one model generalizes across modalities, e.g., depth completion across LiDAR/ToF Park et al. [2024], 3D reconstruction across fisheye and rolling-shutter cameras Wu et al. [2025], and video generation across diverse optics Zhang et al. [2025]. In the RAW/ISP domain, well-documented cross-sensor variation in spectral sensitivity Jiang et al. [2013] and radiometric response Healey and Kondepudy [2002] has motivated camera-prior approaches such as unpaired RAW-to-RAW translation Perevozchikov et al. [2024], parameter-aware forward/inverse ISPs Kim et al. [2023], and metadata/EXIF-conditioned models Afifi et al. [2025], Zheng et al. [2023]. Unlike these, we target sensor-agnostic RAW *detection*, addressing bit depth, spectral sensitivity, and exposure via a physics-guided global-local framework.

3 Method

3.1 Motivation

Many of the factors discussed in the introduction collapse along common axes. The illuminant spectrum and camera spectral response jointly control the per-channel color balance, i.e., color temperature and tint. Scene radiance, shutter time, and analog gain together scale the overall signal level, i.e., exposure. The sensor’s non-linear response and ADC bit depth govern tonal compression and quantization at highlights and shadows. We train a linear-RAW-stem detector on three RAW

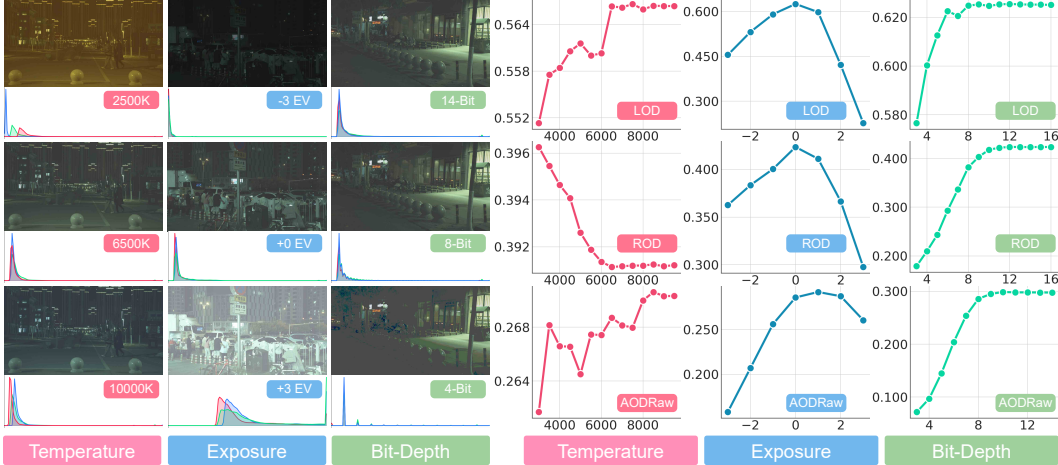


Figure 3: Sensitivity of RAW object detection to environmental and sensor-induced variations. Left: three AODRAW frames rendered under shifted illumination color temperature, exposure, and sensor bit depth, each paired with its pixel histogram. Right: mAP50 of a pretrained ResNet50 backbone with a linear RAW stem on LOD, ROD, and AODRAW as the three factors sweep across their ranges.

benchmarks [Hong et al. \[2021\]](#), [Xu et al. \[2023\]](#), [Li et al. \[2025b\]](#) and evaluate it under controlled shifts along each axis. As shown in Figure 3, detection accuracy drops sharply along all three once the input deviates from the training capture setting; a sensor-agnostic detector must therefore absorb variation along all of them. These distortions act at two scales: a global tonal shift from illuminant, exposure, and sensor non-linearity, and local color perturbations from mixed illumination, lens-shading falloff, and cross-channel crosstalk.

We factor the adapter into two physically meaningful operators: (i) a global per-channel curve g that absorbs color temperature, exposure, and bit-depth shifts via a single monotone function, and (ii) a spatially- and luminance-adaptive color translation matrix M that handles residual local errors. The output y then takes the form:

$$y(p) = M(p, \ell(p)) g(I(p)), \quad \ell(p) = \frac{1}{3} \sum_c I_c(p), \quad (1)$$

where $I, y \in [0, 1]^{3 \times H \times W}$ are the normalized linear RAW input (after black-level subtraction) and the backbone-ready output. Crucially, $\ell(p)$ is computed from the unmapped I rather than $g(I)$, so its luminance axis retains a fixed physical meaning across sensors and training stages. We parameterize g as a degree- n Bézier curve (Section 3.2) and store M as a low-resolution Bilateral Grid (Section 3.3); both are jointly predicted by a shared histogram-guided network (Section 3.4).

3.2 Global Differentiable Bézier Curve

As illustrated on top of Figure 4, the global tone curve g maps the linear RAW signal through a smooth, per-channel monotone function, absorbing exposure, sensor non-linear response, and per-channel sensitivity into $3(n-1)$ scalar coefficients. We parameterize g as a degree- n Bézier curve per channel [Serrano-Lozano et al. \[2024\]](#), which is pointwise bounded, monotone under ordered control points, and pinned to pure black and white at its endpoints. Let $\{p_{c,i}\}_{i=0}^n \subset [0, 1]$ denote the $n+1$ control points for channel $c \in \{R, G, B\}$. Given $t = I_c(p) \in [0, 1]$, the curve evaluates pointwise as:

$$g_c(t) = \sum_{i=0}^n B_{n,i}(t) p_{c,i}, \quad B_{n,i}(t) = \binom{n}{i} (1-t)^{n-i} t^i, \quad (2)$$

where $\{B_{n,i}\}_{i=0}^n$ are the Bernstein basis polynomials. Since $B_{n,i}(t) \geq 0$ and $\sum_i B_{n,i}(t) = 1$, each $g_c(t)$ is a convex combination of its control points and stays within $[\min_i p_{c,i}, \max_i p_{c,i}]$. The derivative of g_c admits the closed form:

$$g'_c(t) = n \sum_{i=0}^{n-1} B_{n-1,i}(t) (p_{c,i+1} - p_{c,i}), \quad (3)$$

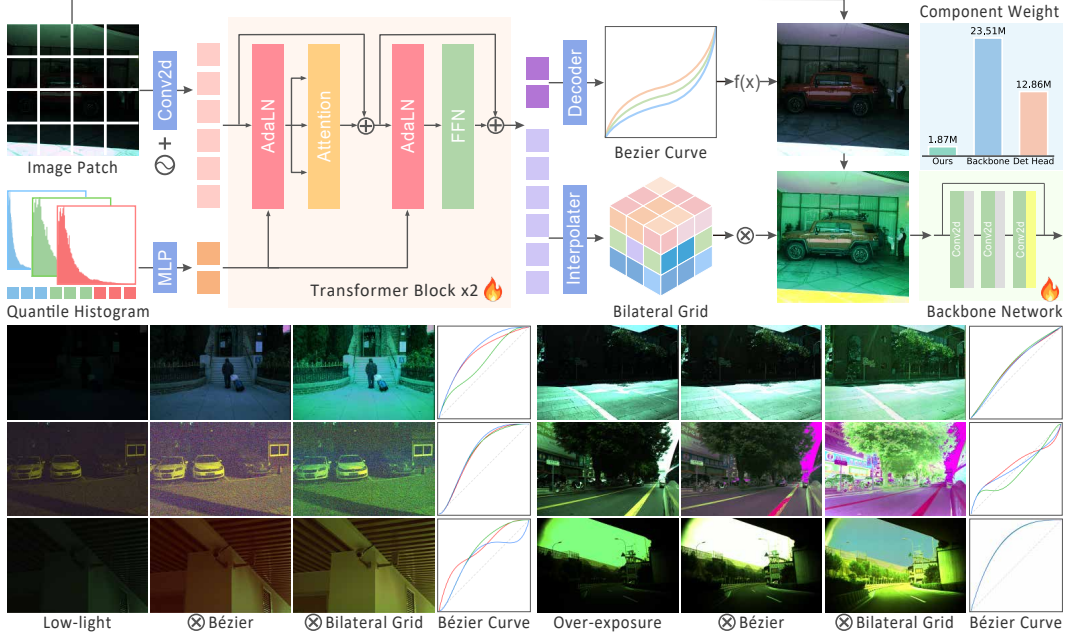


Figure 4: Overall architecture of the proposed method. A RAW image and its quantile histogram drive transformer blocks via AdaLN, jointly predicting a global Bézier curve $f(x)$ and a Bilateral Grid for local color correction. Qualitative examples on low-light and over-exposed inputs show the Bézier-only output, the full Bilateral Grid output, and the learned curve.

which is a convex combination of adjacent control-point differences. It stays non-negative under ordered control points $p_{c,0} \leq \dots \leq p_{c,n}$ and renders g_c monotonically non-decreasing. To regularize the predicted curve toward this ordered regime, we anchor the interior points on the uniform ramp $\bar{p}_{c,i} = i/n$ and apply a bounded residual that keeps each update a bounded perturbation of identity as:

$$p_{c,i} = \text{clip}_{[0,1]} \left(\frac{i}{n} + \frac{1}{2} \tanh(\delta_{c,i}) \right), \quad i = 1, \dots, n-1. \quad (4)$$

Our Bézier parameterization is both more expressive than a per-channel gamma [Xie et al. \[2026\]](#), whose single scalar cannot fit the S-shaped response of modern sensors, and more constrained than free-form polynomial bases [Guo et al. \[2025\]](#), which provide no endpoint or monotonicity guarantees and may crush or invert tones near black and white. Because $\delta_{c,i}$ is predicted per image from sensor-dependent statistics in Section 3.4, g specializes adaptively across sensors. A wide-dynamic-range Bayer sensor receives an aggressively compressive curve, whereas a narrow-range low-bit sensor receives a near-linear one. The $3(n-1)$ learned degrees of freedom thus absorb exposure, gamma, and per-channel sensitivity differences without any sensor-specific architecture.

3.3 Local Bilateral Grid Color Transform

The global curve leaves spatially-varying color shifts intact. A single RAW frame routinely contains mixed illumination, lens-shading falloff, and sensor-dependent crosstalk. Detection does not require a colorimetrically faithful image, but benefits from enhanced local contrast and balanced color that expose object boundaries and textures to the backbone. We therefore apply a spatially-adaptive 3×3 color transform, represented as a bilateral grid following [Chen et al. \[2007\]](#), [Gharbi et al. \[2017\]](#), as depicted in the bottom of Figure 4.

Grid Representation and Trilinear Slicing. The grid $\mathbf{G} \in \mathbb{R}^{9 \times G_d \times G_h \times G_w}$ stores the nine coefficients of a 3×3 matrix at each cell, with spatial resolution $(H/16) \times (W/16)$ and $G_d=8$ luminance bins. Each full-resolution pixel p recovers its coefficients by trilinear interpolation into \mathbf{G} at the continuous coordinate $(xG_w/W, yG_h/H, \ell(p)G_d)$,

$$m(p) = \sum_{(d,h,w) \in \mathcal{N}(p)} w_d(p) w_h(p) w_w(p) \mathbf{G}_{:,d,h,w} \in \mathbb{R}^9, \quad (5)$$

where $\mathcal{N}(p)$ is the eight enclosing grid vertices and (w_d, w_h, w_w) are the linear interpolation weights. The sampled vector reshapes into a 3×3 matrix $M(p)$ and applies pointwise as:

$$y(p) = \text{clip}_{[0,1]}(M(p)g(I(p))). \quad (6)$$

Prediction operates at grid resolution and rendering is $\mathcal{O}(HW)$, so the luminance axis lets pixels at the same location but different brightness sample different matrices without per-pixel prediction cost.

Structured Matrix Parameterization. A free 3×3 prediction at every cell is fragile in practice. Sensor-to-sensor color differences are dominated by per-channel gain absorbing white balance, RAW-domain exposure, and spectral-sensitivity scaling, which can vary by a factor of three or more across illuminants and sensors. Channel mixing absorbs residual cross-spectral overlap and color-filter leakage, and is a small correction of at most 10 to 20% relative to the dominant channel [Karaimer and Brown \[2016\]](#). An unconstrained 3×3 conflates these two effects at markedly different magnitudes. Gradients on the dominant gain contaminate the off-diagonals, and early-iteration matrices that are ill-conditioned or sign-flipped destroy the pretrained backbone’s features. We therefore parameterize every cell of \mathbf{G} as:

$$M = D(I + A), \quad D = \text{diag}(d), \quad d = \exp(\tanh(\hat{d})), \quad A_{ij|i \neq j} = k \tanh(\hat{a}_{ij}), \quad (7)$$

where $\hat{d} \in \mathbb{R}^3$ and $\hat{a} \in \mathbb{R}^6$ are the nine raw coefficients emitted by the prediction network, with fixed activation bound $k=0.05$. The matrix takes the explicit form:

$$M = \begin{bmatrix} d_1 & d_1 A_{12} & d_1 A_{13} \\ d_2 A_{21} & d_2 & d_2 A_{23} \\ d_3 A_{31} & d_3 A_{32} & d_3 \end{bmatrix}, \quad (8)$$

in which each row is a gain d_i multiplied by a unit-diagonal mixing vector. The diagonal entries lie in $[e^{-1}, e^1] \approx [0.37, 2.72]$, so d neither collapses to zero nor flips sign, and color channels retain their physical orientation throughout training. With $|A_{ij}| \leq k$, the matrix $I + A$ is strictly diagonally dominant and invertible, and so is $M = D(I + A)$, which prevents the detector backbone from observing degenerate inputs. Left-multiplication by D further ensures that A encodes mixing ratios relative to each row’s gain rather than absolute channel deltas, so globally rescaling a channel adjusts only d_i and leaves A invariant. This decoupling eliminates the gradient interference between exposure and color-mixing corrections that plagues unconstrained 3×3 predictions.

Zero-initializing the grid head gives $\hat{d}=\hat{a}=\mathbf{0}$, hence $d=\mathbf{1}$, $A=\mathbf{0}$, and $M=I$. Combined with the identity-initialized Bézier curve of Equation (4), the full adapter Equation (1) is exactly the identity at initialization and thereafter learns a bounded, well-conditioned residual, allowing a single network to train jointly across heterogeneous sensors.

3.4 Histogram-Guided Curve and Grid Prediction

The Bézier residual δ and the Bilateral Grid \mathbf{G} are predicted by a single shared network from the normalized linear RAW input I . Four stride-2 3×3 convolutions with channel progression $3 \rightarrow 32 \rightarrow 64 \rightarrow 128 \rightarrow D$ produce a token map of shape $D \times G_h \times G_w$, which is augmented with fixed 2D sin-cos positional encodings [Vaswani et al. \[2017\]](#) and refined by two transformer blocks.

To inject sensor-level priors, we compute a differentiable per-channel quantile descriptor $\mathbf{q} \in \mathbb{R}^{3 \times Q}$ with $Q=64$ entries per channel as a differentiable surrogate of the channel histogram, where for each rank $r \in \{1, \dots, Q\}$ the entry q_r is the r/Q -th empirical quantile of the pixel intensities, obtained via soft sorting for end-to-end differentiability, and project it through a small MLP to produce per-layer AdaLN [Peebles and Xie \[2023\]](#) scale and shift parameters. These modulate the attention and FFN activations of each block, so the same network adapts to sensor statistics such as bit depth, white-balance bias, exposure regime, and dynamic-range occupancy. The descriptor is equivariant to monotone rescalings of the signal, so relative spacings between successive q_r rather than absolute values encode distribution shape, yielding robustness across heterogeneous bit depths and gains.

A 1×1 convolution expands each spatial token into $G_d \cdot 9$ raw grid coefficients, reshaped and passed through Equation (7) to yield \mathbf{G} . A linear head maps the average-pooled token features to the Bézier residual δ , combined with the uniform anchor via Equation (4). Only the convolutional stem depends on HW , so the adapter adds a near-constant per-image cost across detector architectures.

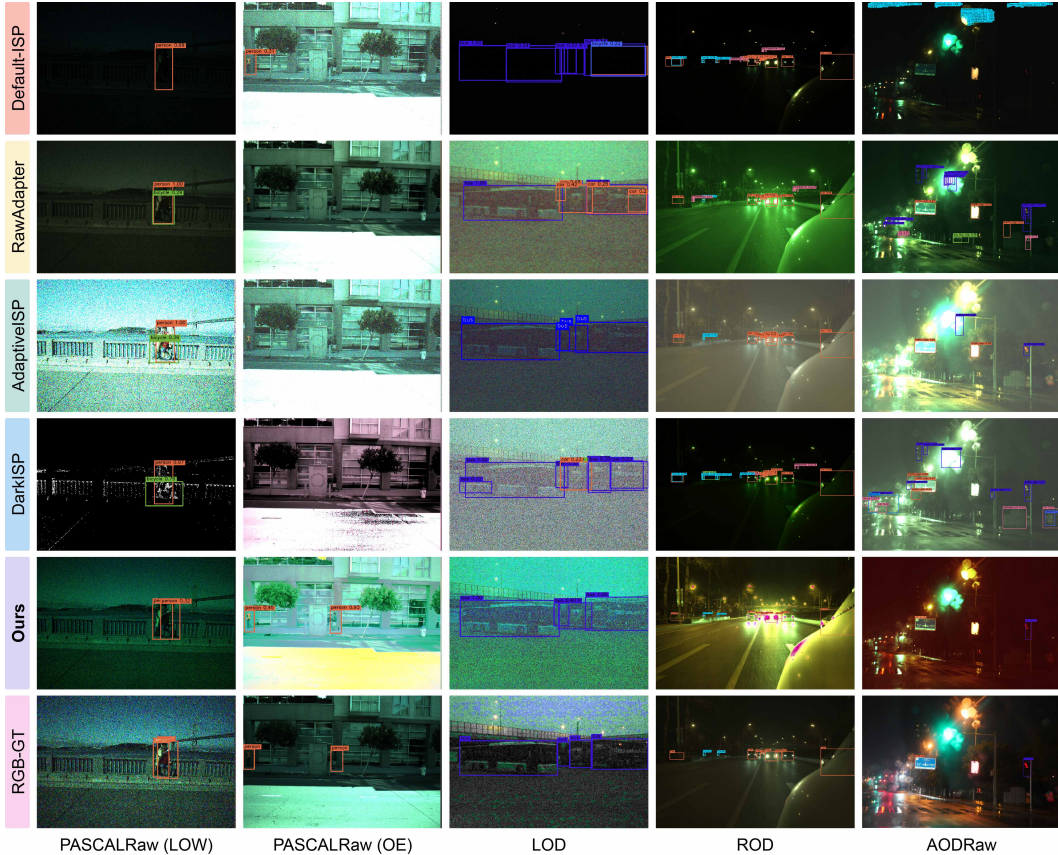


Figure 5: Qualitative comparison of object detection on PASCALRAW Omid-Zohoor et al. [2017], LOD Hong et al. [2021], ROD Xu et al. [2023], and AODRAW Li et al. [2025b]. Our method produces more robust and accurate detections than the baselines. Zoom in for details.

4 Experiment

Implementation Details We implement our models in PyTorch with MMDetection. We loaded pretrained RetinaNet for all baseline methods, finetuned with SGD ($\text{lr } 1 \times 10^{-3}$, momentum 0.9, weight decay 5×10^{-4}) for 20 epochs at batch size 4, with a 500 step linear warmup. Augmentation consists of resizing and random horizontal flipping ($p=0.5$). Figure 4 (upper right) reports the parameter breakdown of the network components, and Table 3 compares inference time and memory against representative baselines using a NVIDIA H100 GPU.

Baseline Methods. We compare our method with default ISP and recent task-oriented ISP approaches, including ReconfigISP Yu et al. [2021], RAW-Adapter Cui and Harada [2024], AdaptiveISP Wang et al. [2024d], Dark-ISP Guo et al. [2025], and Dr.RAW Huang et al. [2025].

Benchmarks. For object detection on RAW images, we use the 12-bit PASCALRAW dataset Omid-Zohoor et al. [2017] and its lowlight (*LOW*), normal (*NM*), and overexposure (*OE*) variants Cui and Harada [2024]. We further adopt the 14-bit AODRAW Li et al. [2025b], 16-bit LOD Hong et al. [2021], and 24-bit ROD Xu et al. [2023] datasets, along with the Multi-RAW dataset Li et al. [2024b] that contains 10-, 12-, 16-, and 24-bit RAW images captured by diverse sensors. We additionally construct a mixed-sensor dataset from PASCALRAW and LOD, and synthesize multi-sensor dataset, with synthesis details provided in the Appendix A. Additional experiments of RAW image segmentation are provided in Appendix C.4.

Metric. We report object detection accuracy in $\text{mAP}@50$ and $\text{mAP}@75$. Best results in experiments are shaded as **first**, **second**, and **third**. Linear-RAW denotes direct integration of RAW images.

Table 1: Evaluation of object detection performance in mAP@50 and @75 on PASCALRAW Low/Normal/Overexposed, LOD, ROD, and AODRAW. Models use a ResNet50 He et al. [2016] or a SwinTransformer Liu et al. [2021] backbone.

Method	PAS.LOW		PAS.NM		PAS.OE		LOD		ROD		AODRAW		
	@50	@75	@50	@75	@50	@75	@50	@75	@50	@75	@50	@75	
ResNet-50	Linear-RAW	0.7668	0.5793	0.8661	0.7273	0.8747	0.7298	0.5710	0.3713	0.3041	0.1963	0.2301	0.1485
	Default-ISP	0.8390	0.6676	0.8959	0.7328	0.8967	0.7333	0.5880	0.3549	0.4178	0.2709	0.3241	0.2063
	ReconfigISP	0.8562	0.6662	0.8949	0.7286	0.8989	0.7263	0.5383	0.2903	0.3436	0.2137	0.2896	0.1763
	RAW-Adapter	0.8647	0.6935	0.8942	0.7270	0.8987	0.7333	0.6082	0.3285	0.3950	0.2560	0.2934	0.1878
	AdaptiveISP	0.8871	0.7293	0.9014	0.7872	0.9011	0.7636	0.6142	0.4071	0.4379	0.2848	0.3382	0.2131
	Dark-ISP	0.7139	0.4663	0.8940	0.7550	0.8840	0.6890	0.5560	0.3630	0.4090	0.2710	0.3240	0.2060
	Dr.RAW	0.8865	0.7305	0.8983	0.7639	0.8982	0.7624	0.6408	0.4399	0.4720	0.3160	0.3630	0.2310
	Ours	0.8910	0.7330	0.9020	0.7690	0.9020	0.7690	0.6909	0.4363	0.5541	0.3752	0.3623	0.2311
Swin-Transformer	Linear-RAW	0.5517	0.3336	0.8707	0.6882	0.8733	0.6196	0.5279	0.2828	0.3251	0.2120	0.1241	0.0768
	DefaultISP	0.8581	0.7156	0.9023	0.7769	0.8966	0.7410	0.6978	0.5015	0.4885	0.3119	0.3428	0.2308
	ReconfigISP	0.8803	0.6999	0.8946	0.7165	0.9017	0.7618	0.5935	0.3746	0.4051	0.2527	0.2977	0.1966
	RAW-Adapter	0.8727	0.7121	0.9017	0.7869	0.8967	0.7546	0.6289	0.4149	0.4386	0.2869	0.3035	0.1985
	AdaptiveISP	0.7830	0.5516	0.8704	0.7239	0.8883	0.7308	0.5990	0.4581	0.4440	0.2711	0.3661	0.2471
	Dark-ISP	0.7233	0.4852	0.9010	0.7672	0.8980	0.7556	0.6303	0.4146	0.5039	0.3273	0.3398	0.2233
	Dr.RAW	0.8814	0.7183	0.8986	0.7591	0.8958	0.7190	0.6950	0.5266	0.4933	0.3192	0.3268	0.2160
	Ours	0.9083	0.7406	0.9342	0.7792	0.9313	0.7921	0.6986	0.5057	0.5191	0.3467	0.4394	0.3263

Table 2: Evaluation on synthetic and real mixed-sensor datasets.

Method	PAS (Syn)		LOD (Syn)		ROD (Syn)		PAS & LOD		Multi-RAW		Inference Method	Time&Mem.	
	@50	@75	@50	@75	@50	@75	@50	@75	@50	@75		ms	GB
Linear-RAW	0.8921	0.7295	0.5310	0.3297	0.3497	0.2273	0.6057	0.4175	0.2539	0.1227	Linear-RAW	7.20	0.23
RAW-Adapter	0.8869	0.7233	0.5874	0.3945	0.3637	0.2397	0.6540	0.4370	0.2334	0.1025	RAW-Adapter	10.00	0.24
Dr.RAW	0.8949	0.7324	0.5924	0.4164	0.4234	0.2821	0.6660	0.4750	0.2572	0.1195	Dr.RAW	10.52	0.53
Dark-ISP	0.8888	0.7334	0.5837	0.3390	0.3703	0.2403	0.6420	0.4360	0.2603	0.1063	Dark-ISP	20.45	0.99
Ours	0.8953	0.7343	0.6646	0.4602	0.4291	0.3223	0.6865	0.4896	0.3528	0.1336	Ours	10.70	0.24

Table 3: Efficiency.

4.1 Evaluation on Per-Sensor Benchmarks

Table 1 reports mAP@50 and mAP@75 across the six per-sensor benchmarks under both a ResNet-50 and a Swin-Transformer backbone. Our adapter achieves superior or competitive performance on all settings. The improvement is more pronounced beyond the conventional 12-bit setting; on ROD and LOD, ResNet-50 mAP@50 improves by 17.4% and 7.8% over the strongest baseline approaches. Across the three PASCALRAW exposure variants constructed by Cui and Harada [2024], the model recovers nearly identical mAP@50 on LOW, NM, and OE, suggesting that the bounded global curve absorbs exposure variation rather than overfitting to a particular setting. Figure 5 shows fewer missed and mislocalized boxes under saturated highlights and severely underexposed regions.

4.2 Evaluation on Mixed-Sensor Benchmarks

Table 2 examines how each method behaves when training and evaluation span heterogeneous sensor captures. Our method attains the highest mAP@50 among task-oriented ISPs in both synthetic and real-world settings, with relative gains of 6.1% on LOD (Syn), 3.1% on PASCALRAW & LOD, and 9.8% on MultiRAW over the strongest baselines. The margin is largest on MultiRAW, which spans the widest range of bit depths and capture devices in our evaluation. On such heterogeneous mixes, previous pipelines tend to fit their parameters to a dominant sensor mode, whereas our histogram-conditioned prediction adapts to per-image statistics through the global Bézier curve and bilateral grid, which generalizes more reliably across sensor configurations.

5 Ablation Study

Ablations are conducted on LOD dataset Hong et al. [2021] with the same ResNet-50 backbone. Figure 6 visualizes the transformed linear images from each ablated module or design.

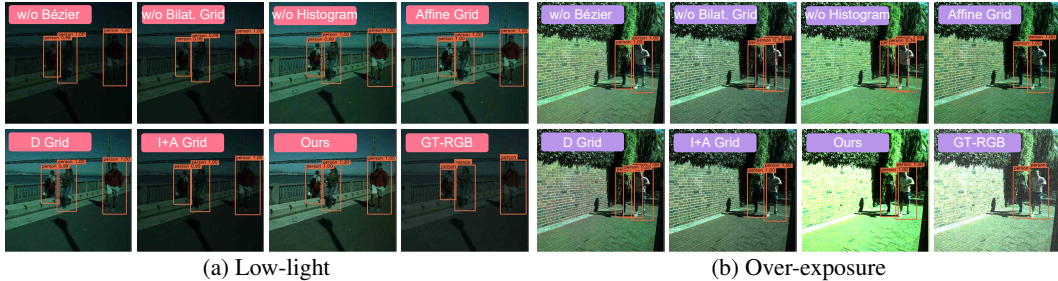


Figure 6: Visualization of ablation studies on PASCALRAW lowlight and overexposure variants. Each case presents transformed images of design choices shown in Table 4, Table 5, and Table 6.

Table 4: Ablation of histogram conditioning mechanisms.

Ablation	@50	@75
No Histogram	0.6838	0.4241
Prefix Condition	0.6397	0.4123
AdaLN Condition	0.6909	0.4363

Table 5: Ablation study of global Bézier curve design.

Ablation	@50	@75
No Bézier	0.6650	0.4133
Vanilla Bézier	0.6511	0.4343
Delta Bézier	0.6909	0.4363

Table 6: Ablation of bilateral grid.

Ablation	@50	@75
No Bilateral Grid	0.6691	0.4346
Vanilla Bilateral Grid	0.6673	0.4149
D	0.6589	0.4461
I+A	0.6646	0.4118
D(I+A)	0.6909	0.4363

Effect of Histogram Conditioning Table 4 compares ways of injecting the input histogram. AdaLN modulation outperforms both removing the histogram and routing it through a prefix token, consistent with the histogram acting as a sensor-level prior that is most useful when it reshapes every block rather than competing with spatial tokens for attention.

Effect of Global Bézier Curve Table 5 compares forms of the global tone curve. Our delta parameterization outperforms both removing the curve and a vanilla Bézier that emits absolute control points, with the vanilla variant falling slightly below the no-curve baseline. This is consistent with the head benefiting from a uniform anchor rather than having to learn the identity transform from scratch on every input. Figure 7a further shows that accuracy plateaus once the curve has enough degrees of freedom to express the typical sensor response.

Effect of Spatial Bilateral Grid Table 6 disentangles the diagonal-mixing decomposition $D(I+A)$. The full form is best, whereas predicting only D or only $I+A$ falls even below the no-grid baseline, suggesting the gain comes from decoupling per-channel exposure and cross-channel mixing rather than from an increase in parameter count. Figure 7b shows that the grid activation bound k defined in Equation (7) is stable across moderate values and degrades at the extremes where the grid approaches the identity or becomes nearly singular.

6 Conclusion

We address sensor-agnostic RAW object detection, where differences in bit depth, spectral response, and exposure across cameras prevent a single detector from generalizing. We factor the adapter into a global Bézier tone curve and a local bilateral grid of structured $D(I+A)$ matrices, both predicted from the input histogram by a shared transformer, and show across per-sensor and mixed-sensor RAW benchmarks that it outperforms previous task-oriented ISPs at near-constant inference cost.

Limitation Real mixed-sensor RAW data with balanced labels remains scarce, so our experiments on natively heterogeneous captures remain challenging to conduct at large scale. Developing such a label-balanced, multi-sensor RAW detection dataset would be a valuable direction for future research.

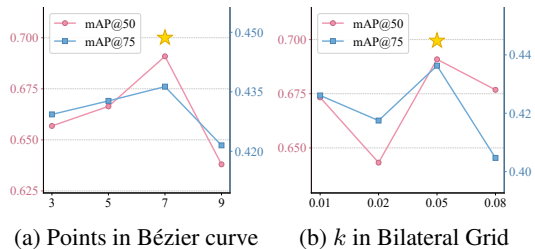


Figure 7: Ablation on grid activation k and the number of Bézier control points. Star is our choice.

A Simulated RAW Augmentation

To improve the generalization of our detection model across heterogeneous imaging conditions, we construct a physics-based RAW image simulation pipeline that synthesizes plausible sensor outputs under diverse camera spectral sensitivities, illuminants, exposures, and sensor characteristics. All operations are performed in linear RAW space after black-level subtraction, and the output is a simulated linear RAW image normalized to $[0, 1]$. Table 2 reports detection results on our synthesized dataset, which is built from PASCALRAW Omid-Zohoor et al. [2017], LOD Hong et al. [2021], and ROD Xu et al. [2023]. We exclude AODRaw Li et al. [2025b] because it already contains diverse real-world degradations such as adverse weather and challenging illumination.

Camera Spectral Sensitivity Database. We use the 28-camera spectral sensitivity database of Jiang et al. [2013], which provides per-channel sensitivity curves $S_c^{(i)}(\lambda)$ for $c \in \{R, G, B\}$ sampled at 33 wavelengths from 400 nm to 720 nm in 10 nm increments. Each curve is peak-normalized to unity. Following Jiang et al. [2013], we observe that the space of real camera sensitivities is well approximated by a low-dimensional linear subspace, and fitting a two-component PCA independently for each channel explains most of the inter-camera variance as shown in Figure 8.

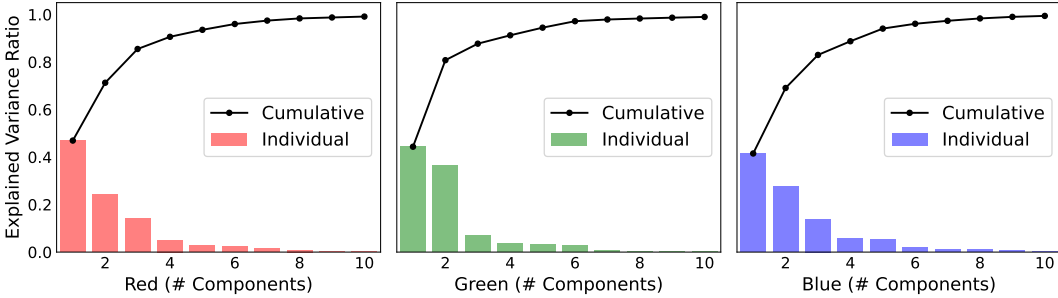


Figure 8: Per-channel PCA explained variance for the 28-camera spectral sensitivity database.

Offline Precomputation. Let $\mathbf{X}^c \in \mathbb{R}^{28 \times 33}$ denote the matrix of peak-normalized sensitivity curves for channel c . We fit PCA with $k = 2$ components as:

$$\mathbf{X}^c = \mathbf{1}(\boldsymbol{\mu}^c)^\top + \mathbf{1}(\boldsymbol{\sigma}^c)^\top \odot \mathbf{Z}^c \mathbf{V}^{c\top} + \mathbf{E}^c, \quad (9)$$

where $\mathbf{V}^c \in \mathbb{R}^{33 \times 2}$ are the principal components and $\mathbf{Z}^c \in \mathbb{R}^{28 \times 2}$ are the corresponding coefficients. We record the per-component empirical mean $\bar{\mathbf{z}}^c$, standard deviation $\hat{\sigma}^c$, and extrema ($\mathbf{z}_{\min}^c, \mathbf{z}_{\max}^c$) from the 28 real cameras.

We also precompute the ColorChecker response of a surrogate source camera. Since the true spectral sensitivity of the source camera is generally unavailable, we approximate it by the mean sensitivity across all 28 cameras:

$$\bar{S}(\lambda) = \frac{1}{28} \sum_{i=1}^{28} S^{(i)}(\lambda). \quad (10)$$

This choice is preferred over the CIE 1931 2° standard observer Commission Internationale de l’Eclairage [2018] as the source proxy. As illustrated in Figure 9, the CIE \bar{z} function peaks at 1.77, well above the typical blue-channel response of real cameras (≈ 0.82), which would artificially suppress the blue-channel dynamic range in the estimated cross-camera matrix. Under D65 illumination Commission Internationale de l’Eclairage [1995], the ColorChecker response of the source proxy is

$$\mathbf{P}_A = (\mathbf{R} \odot \mathbf{d}_{65} \mathbf{1}^\top)^\top \bar{\mathbf{S}} \cdot \Delta\lambda \in \mathbb{R}^{24 \times 3}, \quad (11)$$

where $\mathbf{R} \in \mathbb{R}^{33 \times 24}$ contains the Macbeth ColorChecker 2005 reflectance spectra McCamy et al. [1976], $\mathbf{d}_{65} \in \mathbb{R}^{33}$ is the D65 spectral power distribution, and $\Delta\lambda = 10$ nm. \mathbf{P}_A is then normalized so that the green column equals unity.

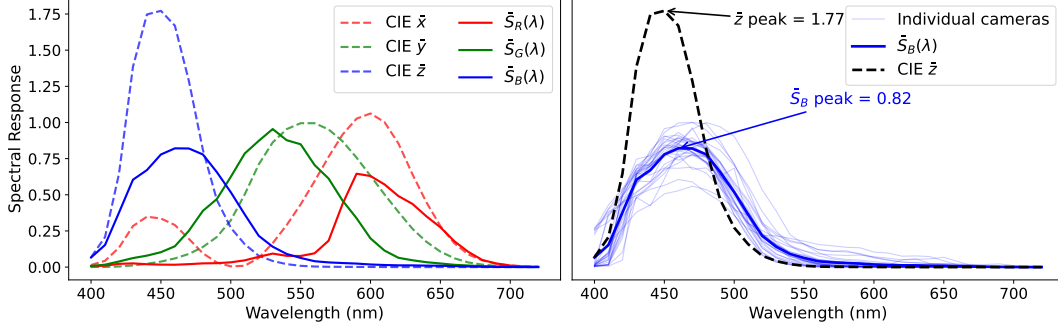


Figure 9: Comparison of the CIE 1931 2° standard observer CMFs (dashed) and the 28-camera mean spectral sensitivity $\bar{S}(\lambda)$ (solid) used as the source camera proxy. The CIE \bar{z} function peaks at 1.77, far above the typical blue-channel response of real cameras (≈ 0.82), motivating our use of $\bar{S}(\lambda)$ to avoid compressing the blue-channel dynamic range in the cross-camera transform.

Exposure Sampling. A global exposure gain α is sampled log-uniformly in stop units:

$$u \sim \mathcal{U}(u_{\min}, u_{\max}), \quad \alpha = 2^u, \quad (12)$$

with $u_{\min} = -3$ and $u_{\max} = 3$, spanning a six-stop dynamic range. This log-uniform prior reflects the fact that perceptually equal exposure steps correspond to multiplicative gains Reinhard et al. [2010].



Figure 10: Visualization of RAW images synthesized using different exposure values (EVs).

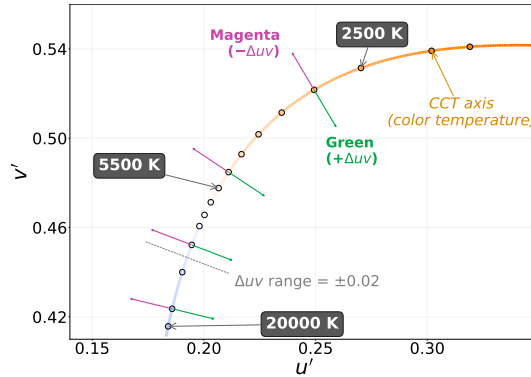


Figure 11: Visualization of Planckian Locus on CIE 1976 $u'v'$ chromaticity diagram.

Color Temperature and Tint Sampling. We sample the illuminant color temperature in the mired scale Priest [1933], also known as the micro-reciprocal degree scale. This parameterization is commonly used for color-temperature shifts because equal steps in mired produce more uniform perceptual changes than equal steps in Kelvin, especially along the Planckian locus Wyszecki and Stiles [2000]. As shown in Figure 11, we uniformly sample the mired value and convert it to the corresponding color temperature as

$$m \sim \mathcal{U}(m_{\min}, m_{\max}), \quad T = \frac{10^6}{m} \text{ K}, \quad (13)$$

with $m_{\min} = 50$ corresponding to $T = 20,000$ K for extreme daylight and $m_{\max} = 400$ corresponding to $T = 2,500$ K for tungsten illumination. Given the sampled temperature, we compute the corresponding spectral power distribution using Planck’s law of black-body radiation [Planck \[1978\]](#),

$$B(\lambda, T) = \frac{2\pi hc^2}{\lambda^5 \left[\exp\left(\frac{hc}{k_B T \lambda}\right) - 1 \right]}, \quad (14)$$

where h is the Planck constant, c the speed of light, and k_B the Boltzmann constant. The resulting spectrum $I_T(\lambda)$ is peak-normalized to unity. Figure 12 illustrates the spectral shift from warm to cool illuminants across the sampled range.

To account for real-world deviations from the ideal Planckian locus, such as those produced by fluorescent or LED sources, we additionally sample a tint offset $\Delta uv \sim \mathcal{U}(-0.04, 0.04)$ along the green–magenta axis of the CIE $u'v'$ uniform chromaticity diagram [CIE \(International Commission on Illumination\) \[1978\]](#). Rather than applying this offset via spectral modification, which requires inverting an overdetermined 33×3 system and yields numerically unstable results, we represent tint as a diagonal RGB gain applied after the cross-camera transform,

$$\mathbf{g}_{\text{tint}} = \left[\max(1 - 0.5 \cdot s \cdot \Delta uv, 0.1), 1.0, \max(1 - s \cdot \Delta uv, 0.1) \right]^\top, \quad (15)$$

where $s = 15.0$ is a fixed scaling constant. The asymmetric weighting, where R receives half the correction of B, prevents over-reddening under strong magenta tints, as reflected in the gain curves shown in Figure 13. The perceptual effects of color temperature and tint variation on a real RAW image are illustrated in Figures 14 and 15, where the simulated illuminant shifts from warm tungsten to cool daylight and from green to magenta across the full sampled ranges.

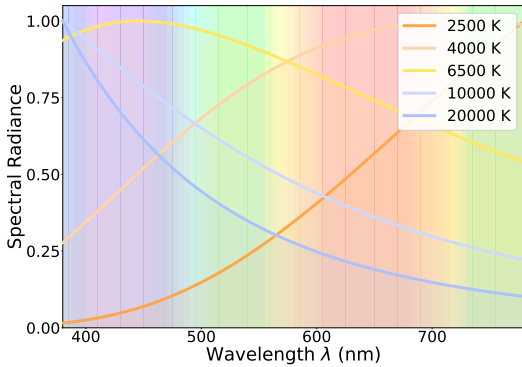


Figure 12: Spectral power distributions $B(\lambda, T)$ of black-body radiators at representative color temperatures spanning our sampling range from 2,500 K to 20,000 K, computed via Planck’s law and peak-normalized to unity.

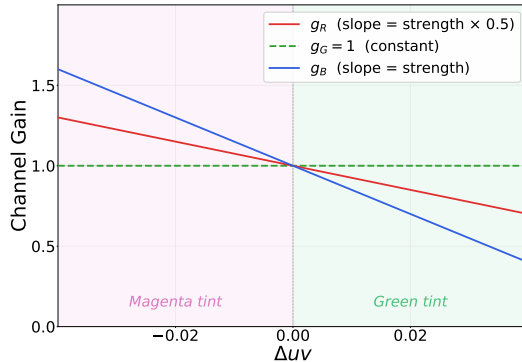


Figure 13: Diagonal RGB gains \mathbf{g}_{tint} as a function of tint offset Δuv . The R channel receives half the correction of the B channel, preventing over-reddening under strong magenta tints while keeping the G gain fixed at unity.



Figure 14: Visualization of color temperature variation on a real RAW image, simulated across the full sampled range from warm tungsten illumination at 2,500 K to extreme cool daylight at 20,000 K.

Target Camera Spectral Response Sampling. A virtual target camera sensitivity $S_B(\lambda) \in \mathbb{R}^{33 \times 3}$ is sampled from the learned low-dimensional manifold. For each channel c , we draw PCA coefficients from a truncated Gaussian:

$$\mathbf{z}^c \sim \mathcal{N}(\bar{\mathbf{z}}^c, \text{diag}(\hat{\sigma}^c)^2), \quad \text{clipped to } [\mathbf{z}_{\min}^c, \mathbf{z}_{\max}^c]. \quad (16)$$

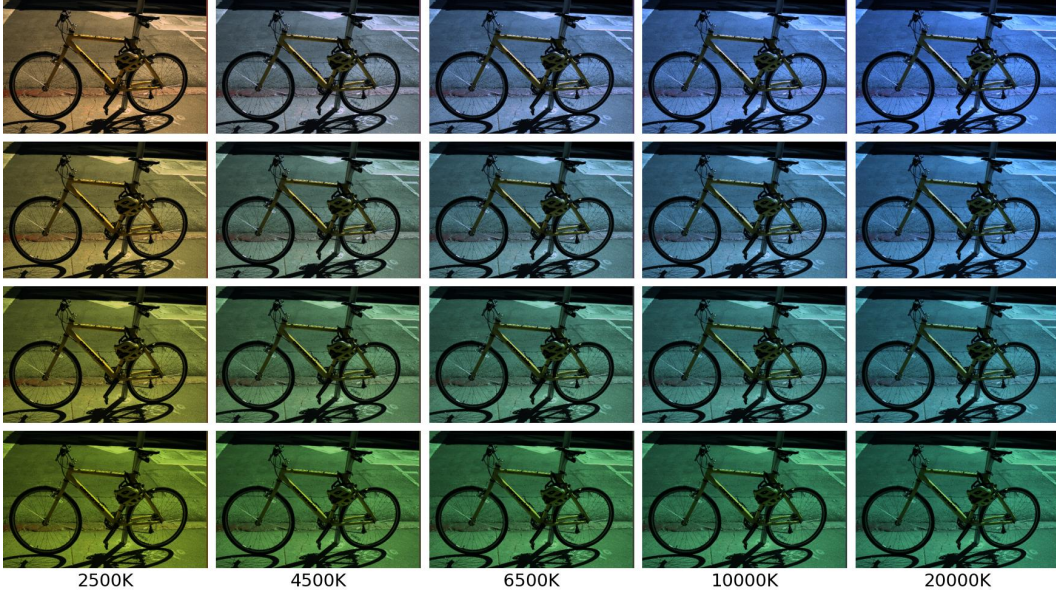


Figure 15: Visualization of temperature and tint variation on a real RAW image, simulated across the full sampled range from strong magenta at $\Delta uv = -0.04$ to strong green at $\Delta uv = +0.04$ along the green–magenta axis of the CIE $u'v'$ chromaticity diagram.

The sensitivity curve is then reconstructed and constrained to be physically realizable:

$$\tilde{S}^c(\lambda) = \sigma^c \odot \mathbf{V}^c \zeta^c + \mu^c, \quad S_B^c(\lambda) = \frac{\max(\tilde{S}^c(\lambda), 0)}{\max_{\lambda} \tilde{S}^c(\lambda) + \epsilon}. \quad (17)$$

The Gaussian prior concentrates samples near the center of the observed camera distribution, while the clipping to $[\mathbf{z}_{\min}^c, \mathbf{z}_{\max}^c]$ ensures the reconstructed curves remain within the convex hull spanned by real cameras. As shown in Figure 16, the synthetic sensitivities faithfully reproduce the shape and spread of the diverse real cameras across all three channels, while providing substantially denser coverage of the plausible sensitivity space.

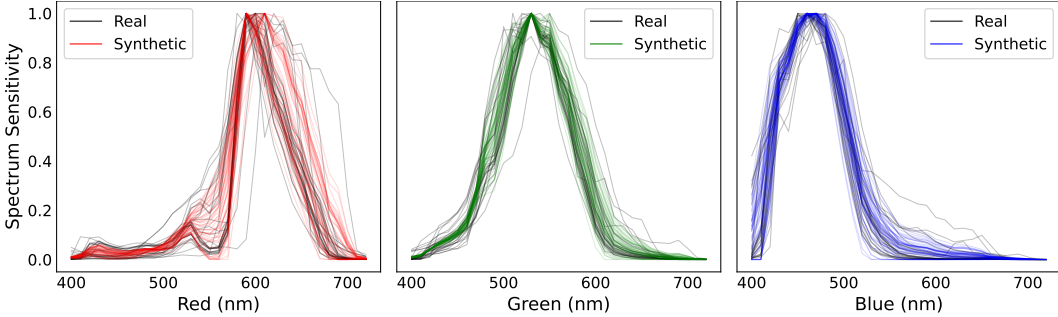


Figure 16: Visualization of spectral sensitivity of real cameras and our synthesized responses.

Cross-camera Color Transform. We compute a 3×3 linear matrix $\mathbf{M}_{A \rightarrow B, T}$ that jointly accounts for the change in camera spectral sensitivity and the change in illuminant from D65 to I_T . The ColorChecker response of the target camera under illuminant I_T is

$$\mathbf{P}_B = (\mathbf{R} \odot I_T \mathbf{1}^\top)^\top \mathbf{S}_B \cdot \Delta\lambda \in \mathbb{R}^{24 \times 3}, \quad (18)$$

normalized so that the green column equals unity. The cross-camera matrix is estimated by least-squares regression over the 24 ColorChecker patches:

$$\mathbf{M}_{A \rightarrow B, T} = \arg \min_{\mathbf{M}} \|\mathbf{P}_A \mathbf{M}^\top - \mathbf{P}_B\|_F^2. \quad (19)$$

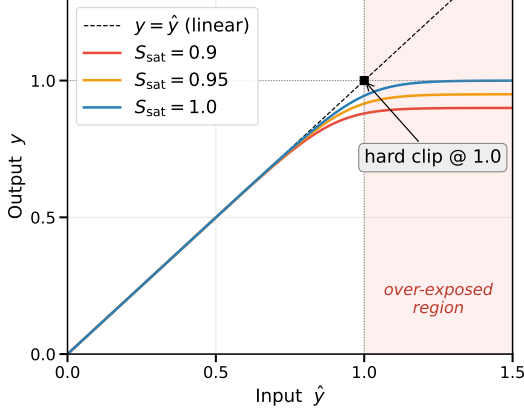


Figure 17: Illustration of the sensor saturation model. For inputs below the saturation threshold S_{sat} , the response follows a smooth compressive curve; beyond this point, the response asymptotically approaches S_{sat} through the tanh roll-off. Lower S_{sat} values produce stronger compression and an earlier onset of saturation.

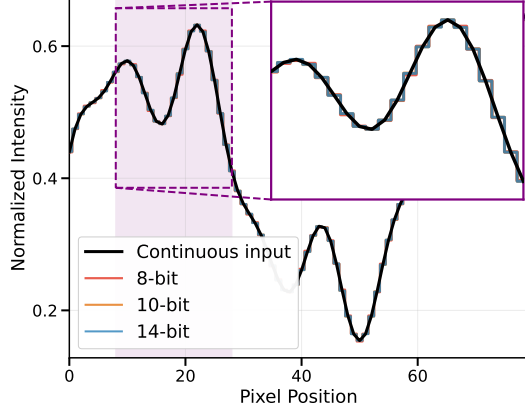


Figure 18: Effect of ADC bit depth on a representative 1D intensity profile. Coarser quantization (8-bit) introduces visible staircase artifacts relative to the continuous reference, while finer quantization (10-bit and 14-bit) progressively recovers the smooth signal shape.

This bridge approach, which uses a reflectance chart to relate two cameras under different illuminants, follows the methodology established in camera color characterization [Barnard et al. \[2002\]](#), [Finlayson \[2013\]](#).

Overall Transformation. Having sampled the exposure α , the cross-camera matrix $\mathbf{M}_{A \rightarrow B, T}$, and the tint gain \mathbf{g}_{tint} , we further model sensor non-idealities via a channel-crosstalk matrix $\boldsymbol{\varepsilon}$, with off-diagonal entries drawn from $\mathcal{U}(-0.05, 0.05)$ and diagonal set to zero, and per-channel black-level offsets $\boldsymbol{\beta} \sim \mathcal{U}(-0.02, 0.02)^3$. Before applying the transform, we remove the inherent green bias of Bayer RAW images via channel-wise white balance:

$$\mathbf{g}_{\text{wb}} = \bar{\mathbf{c}}_G / \bar{\mathbf{c}}, \quad \mathbf{x}_{\text{bal}} = \mathbf{x} \odot \mathbf{g}_{\text{wb}}, \quad (20)$$

where $\bar{\mathbf{c}}$ denotes per-channel spatial means. The full transform matrix is then assembled as

$$\mathbf{M}_{\text{full}} = \alpha(\text{diag}(\mathbf{g}_{\text{tint}}) \mathbf{M}_{A \rightarrow B, T} + \boldsymbol{\varepsilon}), \quad (21)$$

and applied pixel-wise:

$$\mathbf{y} = \mathbf{M}_{\text{full}} \mathbf{x}_{\text{bal}} + \boldsymbol{\beta}. \quad (22)$$

The white balance is then reversed using target camera B's own gray-world multipliers $\mathbf{g}_{\text{wb}}^B = \mathbf{r}_{B, G} / \mathbf{r}_B$ with $\mathbf{r}_B = \mathbf{S}_B^\top I_T \cdot \Delta\lambda$, rather than the source camera's \mathbf{g}_{wb} , so that the output retains target camera B's natural green dominance under illuminant I_T rather than re-imprinting the source camera's spectral bias:

$$\hat{\mathbf{y}} = \mathbf{y} \odot \mathbf{g}_{\text{wb}}^B. \quad (23)$$

Highlight Roll-off and Quantization. To simulate the soft saturation behavior of real sensors approaching full-well capacity [Healey and Kondepudy \[2002\]](#), we apply a tanh-based roll-off:

$$\hat{\mathbf{y}}' = S_{\text{sat}} \tanh\left(\frac{\hat{\mathbf{y}}}{S_{\text{sat}}}\right), \quad S_{\text{sat}} \sim \mathcal{U}(0.9, 1.0), \quad (24)$$

where the tanh function provides a smooth asymptotic upper bound that approaches but never exceeds S_{sat} , while any sub-zero values arising from the black-level offset $\boldsymbol{\beta}$ are clipped to zero, as illustrated in Figure 17. Finally, the output is quantized to a bit depth $b \in \{10, 12, 14, 16\}$ chosen uniformly at random:

$$\tilde{\mathbf{y}} = \frac{1}{2^b - 1} \left\lfloor \frac{\hat{\mathbf{y}}'}{S_{\text{sat}}} (2^b - 1) + 0.5 \right\rfloor, \quad (25)$$

where the floor operation is applied element-wise. The effect of bit depth on signal fidelity is shown in Figure 18. Since every operation is a pointwise color transformation with no spatial warping, ground-truth bounding box annotations remain valid without modification.

B Additional Related Works

RAW Imaging Pipelines for High-Level Vision. Early reconfigurable imaging pipelines [Buckler et al. \[2017\]](#) demonstrate that bypassing most ISP stages preserves the accuracy of CNN-based vision while reducing sensor power, motivating the use of RAW data as a direct input to perception networks. Subsequent works learn end-to-end pipelines that fuse a lightweight neural front end with a downstream classifier or detector [Diamond et al. \[2021\]](#), [Yoshimura et al. \[2023\]](#), [Cui et al. \[2025\]](#). Beyond accuracy, RAW data also provides natural robustness signals, with [Zhang et al. \[2022\]](#) mapping RGB inputs through a learned RAW-domain ISP to defend against adversarial perturbations across classification, segmentation, and detection.

Low-Light RAW Object Detection. Low-light scenarios drive a substantial body of RAW-specific detection research. [Sasagawa and Nagahara \[2020\]](#) merges a learned dark-image enhancer with YOLO via glue layers and knowledge distillation. [Cui et al. \[2021\]](#) introduces a multitask auto-encoding-transformation framework that disentangles ISP and illumination factors from object features. [Hashmi et al. \[2023\]](#) learns hierarchical feature enhancers trained jointly with the detector, while [Hong et al. \[2024\]](#) extracts illumination-invariant kernels grounded in the Lambertian image-formation model. Beyond static images, [Wang et al. \[2024a\]](#) addresses multi-object tracking on dark RAW video with adaptive low-pass downsampling and degradation-suppression learning.

RAW Segmentation and Other High-Level Tasks. Beyond object detection, RAW data has been studied for additional high-level tasks. [Chen et al. \[2023\]](#) performs instance segmentation directly on RAW low-light captures with feature-noise suppression, smooth convolutions, and a paired LIS benchmark. [Sun et al. \[2023\]](#) formulates shadow detection on RAW HDR data through a many-to-many adaptive illumination mapping that preserves multi-scale contrast often lost after ISP tone compression. These efforts show that the linear photon evidence retained in RAW captures benefits dense prediction tasks well beyond bounding-box detection.

sRGB-to-RAW Reconstruction. A complementary research thread reverses the camera pipeline to synthesize realistic RAW from sRGB inputs, enabling RAW-side training without paired sensor captures. The unprocessing framework [Brooks et al. \[2019\]](#) inverts each ISP step in closed form to render large RGB datasets back to the sensor domain for raw denoiser training at scale. CycleISP [Zamir et al. \[2020\]](#) introduces a cycle-consistent learned ISP and inverse-ISP pair that produces realistic noisy RAW for image restoration. Invertible ISP [Xing et al. \[2021\]](#) replaces the camera pipeline with a normalizing flow whose forward pass renders sRGB and inverse pass recovers near-perfect RAW with no metadata. A parallel line stores compact metadata alongside sRGB to anchor accurate per-pixel reconstruction, evolving from raw-reconstruction-aware sRGB compressors [Punnappurath and Brown \[2019\]](#) and spatially-aware sample pairs [Punnappurath and Brown \[2021\]](#) to content-aware metadata [Nam et al. \[2022\]](#) and end-to-end learned latent metadata [Wang et al. \[2023, 2024c\]](#), with a recent extension to video sequences [Zhang et al. \[2024\]](#).

Synthetic RAW for Downstream Tasks. Synthesized RAW data has been widely used to scale learning beyond paired captures. Physics-based noise modeling [Wei et al. \[2020\]](#) calibrates sensor shot, read, row, and quantization noise to match real low-light RAW statistics. Neural Camera Simulators [Ouyang et al. \[2021\]](#) learn a controllable RAW synthesizer conditioned on capture parameters such as exposure and ISO. Day-to-night RAW synthesis [Punnappurath et al. \[2022\]](#) relights daytime RAW captures into nighttime variants for training neural ISPs. ReRAW [Berdan et al. \[2025\]](#) reconstructs sensor-specific RAW from large RGB datasets via stratified sampling for efficient detector pre-training on edge sensors. These inverse-ISP and synthetic-RAW designs are complementary in spirit to our physics-based simulation, while our adapter focuses on a richer global-local tonal representation conditioned on per-image RAW statistics.

RAW for Scientific Imaging. Beyond consumer photography, RAW captures play a central role in scientific instruments where every photon carries quantitative meaning. In fluorescence microscopy,

content-aware image restoration [Weigert et al. \[2018\]](#) pioneered the use of deep networks on raw microscope volumes for denoising and isotropy recovery, followed by label-free virtual fluorescence prediction from transmitted light [Ounkomol et al. \[2018\]](#), cross-modality super-resolution [Wang et al. \[2019\]](#), accelerated single-molecule localization microscopy [Ouyang et al. \[2018\]](#), [Nehme et al. \[2020\]](#), [Speiser et al. \[2021\]](#), Fourier-channel attention super-resolution [Qiao et al. \[2021\]](#), and three-dimensional residual channel attention denoising [Chen et al. \[2021\]](#), all surveyed in [Belthangady and Royer \[2019\]](#). In astronomy, deep networks operate directly on raw CCD frames for galaxy-scale gravitational lensing analysis [Hezaveh et al. \[2017\]](#), self-supervised denoising of ground-based images [Liu et al. \[2025e\]](#), and self-supervised spatiotemporal denoising that pushes deeper detection limits [Guo et al. \[2026\]](#). Closer to our setting, physics-based CCD noise modeling tailored to deep-sky observation [Liu et al. \[2026c\]](#) and conservative flow-matching for ground-to-space astronomical super-resolution [Liu et al. \[2026b\]](#) demonstrate that the linear photon evidence retained in scientific RAW captures supports both restoration and downstream measurement. These developments underline that sensor-agnostic RAW modeling, the focus of our work, is increasingly relevant across imaging domains far beyond ordinary RGB photography.

Broader sRGB Image Processing. In the 2D image domain, recent work spans data-centric denoising [Chang et al. \[2026a\]](#), training-free ensembling [Chang et al. \[2026b\]](#), and adverse-condition image enhancement [Ge et al. \[2026b\]](#). In remote sensing, infrared image super-resolution has been explored [Ge et al. \[2026a\]](#). In 3D vision, related efforts cover neural field rendering with media interaction [Liu et al. \[2025d\]](#), structural-prior multi-view reconstruction [Liu et al. \[2025c\]](#), scene reconstruction under adverse weather [Liu et al. \[2025b\]](#), and physically-degraded multi-view benchmarks [Liu et al. \[2025a, 2026a\]](#). These pipelines operate on three-channel or multi-view RGB inputs rather than RAW image domains.

C Additional Experimental Details and Results

This section summarizes the data curation and shared evaluation protocol used for MultiRAW in our mixed-sensor experiments, and provides more visualizations for the RAW object detection experiments in Section 4, supplementary qualitative results from the LOD ablation study in Section 5, and additional experiments on RAW image segmentation using the ADE20K dataset [Zhou et al. \[2019\]](#).

C.1 MultiRAW Dataset

MultiRAW [Li et al. \[2024b\]](#) is a multi-device RAW detection benchmark of 7,208 images captured by the four sensors ASI_294MCPPro, Huawei_P30Pro, iPhone_XSMax, and OnePlus_5T, spanning heterogeneous CFA patterns, resolutions, and bit depths ranging from 10 to 24 bits, and accompanied by per-sensor ISP renderings and XML annotations.

However, the MultiRAW dataset [Li et al. \[2024b\]](#) exhibits severe cross-sensor class imbalance. For instance, the sensor `oneplus_5t` appears only in the test split. The 11-class taxonomy is also long-tailed and device-coupled, and contains ambiguous overlapping categories such as the merged `bicycle`, `motorcycle`, and `tricycle`. We further observe label misalignment on `huawei_p30pro`, where the ground-truth annotations are shifted from the actual objects in the RAW images.

To address these problems, we build a unified preprocessing pipeline that re-associates RAW images with metadata and corrects label misalignment. Specifically, we keep the original data split intact and select the top-five classes shared across all four sensors, namely `car`, `traffic-sign`, `traffic-light`, `person`, and `bicycle`, and rebalance categories by randomly sampling each class. This yields a class-balanced MultiRAW subset of 3,500 training images and 2,064 test images, on which all baselines are trained and evaluated as shown in Table 2.

C.2 Additional Qualitative Results for RAW Object Detection

We show qualitative results on three RAW detection benchmarks that together span the main difficulties of in-the-wild RAW imaging. AODRAW [Li et al. \[2025b\]](#) covers diverse indoor and outdoor scenes under challenging illumination and adverse weather, including rain, haze, low light, and reduced contrast. LOD [Hong et al. \[2021\]](#) focuses on extremely low-light indoor scenes where

Table 7: Semantic segmentation on RAW ADE20K dataset Zhou et al. [2019] with MiT-series backbones Xie et al. [2021], evaluated by mIoU.

Method	LOW			NM			OE		
	B0	B3	B5	B0	B3	B5	B0	B3	B5
Linear-RAW	0.2027	0.3538	0.3653	0.2632	0.4403	0.4546	0.2691	0.4229	0.4404
RAW-Adapter	0.1885	0.3453	0.3636	0.2939	0.4457	0.4541	0.2683	0.4284	0.4385
Dr.RAW	0.2206	0.3581	0.3821	0.3134	0.4477	0.4666	0.2929	0.4343	0.4475
Dark-ISP	0.2202	0.3559	0.3806	0.3131	0.4432	0.4680	0.2917	0.4283	0.4488
Ours	0.2872	0.3957	0.4082	0.3534	0.4516	0.4708	0.3372	0.4381	0.4560

signal-to-noise ratio is the dominant bottleneck. ROD Xu et al. [2023] consists of automotive driving scenes captured in 24-bit HDR RAW, exposing methods to wide dynamic range and strong highlight or shadow regions typical of day and night traffic. Figure 19 visualizes predictions from our method alongside task-oriented ISP baselines on representative images from each dataset. Across these cases, our method yields cleaner boxes and more stable localization, with fewer missed instances in dark regions, fewer false positives under haze and rain, and tighter fits on small or low-contrast objects in HDR driving scenes.

C.3 Additional Qualitative Results for Ablation Study

Figure 20 visualizes the ablation variants on representative real LOD Hong et al. [2021] samples spanning the three exposure regimes of low-light, normal, and over-exposure. For each regime we show the same scene processed by every ablated configuration alongside our full model and the ground-truth annotations. Removing the Bézier curve leaves the global tonal range poorly aligned, so detections in dark or saturated areas drift or disappear. Replacing our $\mathbf{D}(\mathbf{I}+\mathbf{A})$ bilateral grid with simpler *Affine*, \mathbf{D} , or $\mathbf{I}+\mathbf{A}$ variants weakens spatially adaptive local refinement and produces inconsistent boxes around small or low-contrast objects. Dropping the histogram conditioning removes sensor-aware cues, an effect most visible under over-exposure where predictions become noisier and less stable. Our full model recovers cleaner tonal structure and yields the most consistent detections across all three regimes, complementing the quantitative ablation in Section 5.

C.4 Additional Qualitative Results for RAW Semantic Segmentation

Implementation Details. We follow the exposure-curated ADE20K Zhou et al. [2019] protocol of RAW-Adapter Cui and Harada [2024], with Low-light (*LOW*), Normal (*NM*), and Over-exposure (*OE*) splits. The network input is an offline-processed 8-bit RGB image derived from RAW data and normalized to $[0, 1]$, following the released protocol. We insert the same histogram-conditioned global-local adapter described in Sections 3.2 to 3.4 into SegFormer with MiT-B0, MiT-B3, and MiT-B5 backbones Xie et al. [2021] and keep the decoder unchanged. We compare with Linear-RAW, RAW-Adapter Cui and Harada [2024], Dr.RAW Huang et al. [2025], and Dark-ISP Guo et al. [2025], the baselines with compatible segmentation implementations under the same MMSegmentation framework.

Training runs for 200k iterations using AdamW (base learning rate 6×10^{-5} , $\beta_1=0.9$, $\beta_2=0.999$, weight decay 0.01), with a 1.5k-iteration linear warmup followed by polynomial decay. We use a global batch size of 16 on a single H100 GPU and apply a $10\times$ learning-rate multiplier to the adapter and decode head. MiT-B0 and MiT-B5 are initialized from the corresponding ImageNet-pretrained SegFormer checkpoints, while MiT-B3 is warm-started from an earlier 120k checkpoint. Data augmentation uses random resize to $(2048, 512)$ with ratio range $[0.5, 2.0]$, random crop to 512×512 , and random horizontal flipping. We report mean Intersection-over-Union (mIoU) with single-scale sliding-window inference and no test-time augmentation.

Quantitative Results. Table 7 reports mIoU across the three exposure splits and three backbone scales. Our method consistently improves over all baselines in every setting. The gain is largest with the lightweight MiT-B0 backbone, where we surpass the strongest baseline by 6.66, 4.00, and 4.43 mIoU points under *LOW*, *NM*, and *OE*, respectively. The global Bézier curve stabilizes image-level tonal and exposure statistics, while the bilateral grid refines boundary-sensitive local



Figure 19: Additional qualitative object detection results on AODRAW [Li et al. \[2025b\]](#), LOD [Hong et al. \[2021\]](#), and ROD [Xu et al. \[2023\]](#). The examples highlight adverse weather, severe low-light noise, and simultaneous highlights and shadows, under which our method produces cleaner detections and more stable localization than prior task-oriented ISP baselines.

color and contrast, so the two components together improve dense prediction without modifying the segmentation decoder.

Qualitative Results. Figure 21 shows qualitative comparisons. Under low-light inputs, baseline methods often produce fragmented semantic regions or lose small objects in dark areas. Under over-exposed inputs, saturated regions and compressed local contrast make object boundaries difficult to

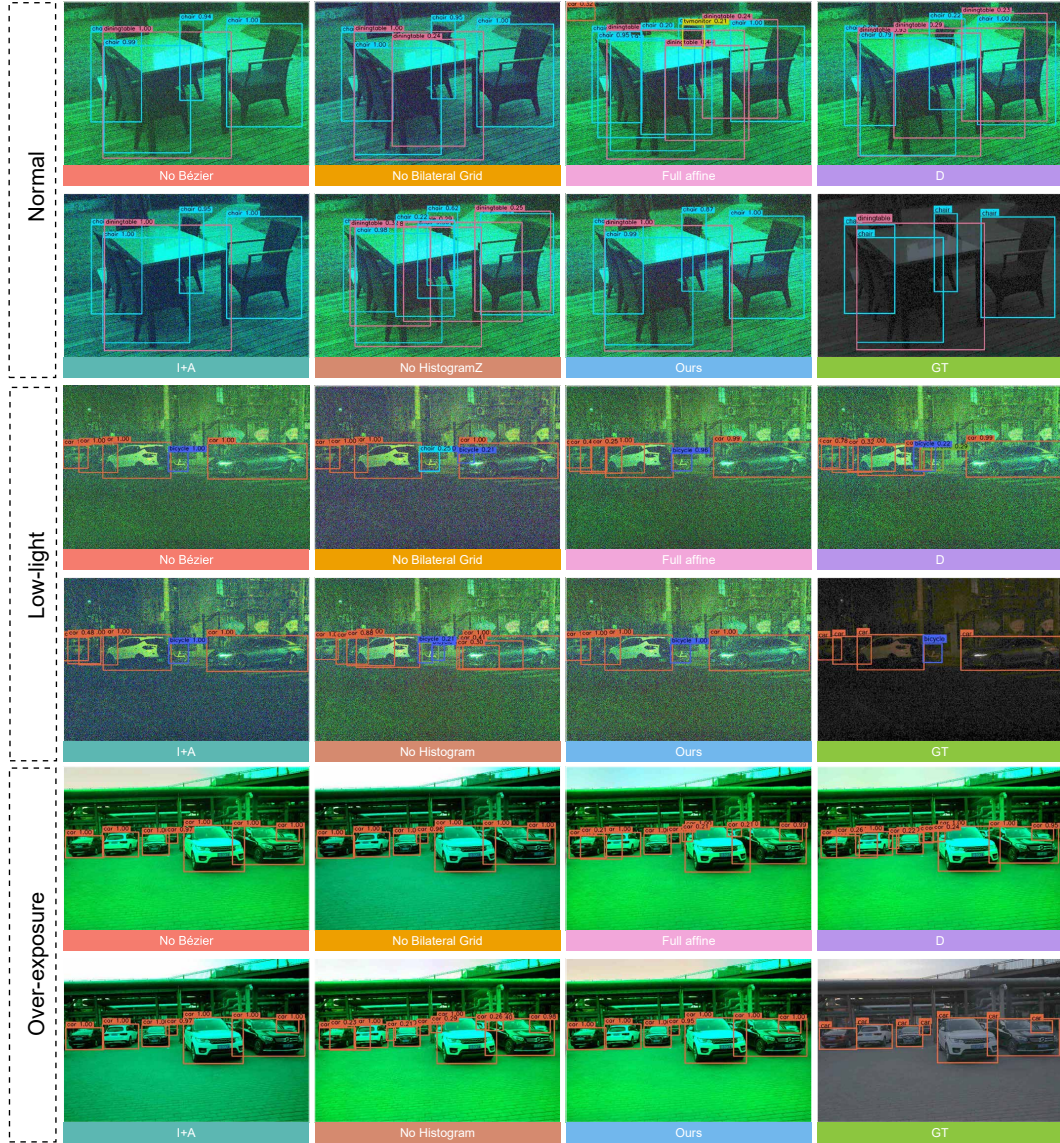


Figure 20: Qualitative ablation on representative real LOD samples under low-light (*LOW*), normal (*NM*), and over-exposure (*OE*) conditions. Each block corresponds to one real LOD exposure regime and compares *w/o Bézier*, *w/o Bilateral Grid*, *Affine Grid*, *D Grid*, *I+A Grid*, and *Ours*. Removing the global curve weakens tonal alignment, removing the bilateral grid harms spatially adaptive local refinement, and removing histogram conditioning reduces sensor-aware robustness. Our full model yields the most stable detections across all settings.

recover. Our method produces more coherent semantic regions and better preserves object boundaries across *LOW*, *NM*, and *OE*, indicating that the same histogram-conditioned global-local adapter transfers from box prediction to dense prediction under RAW exposure variation.

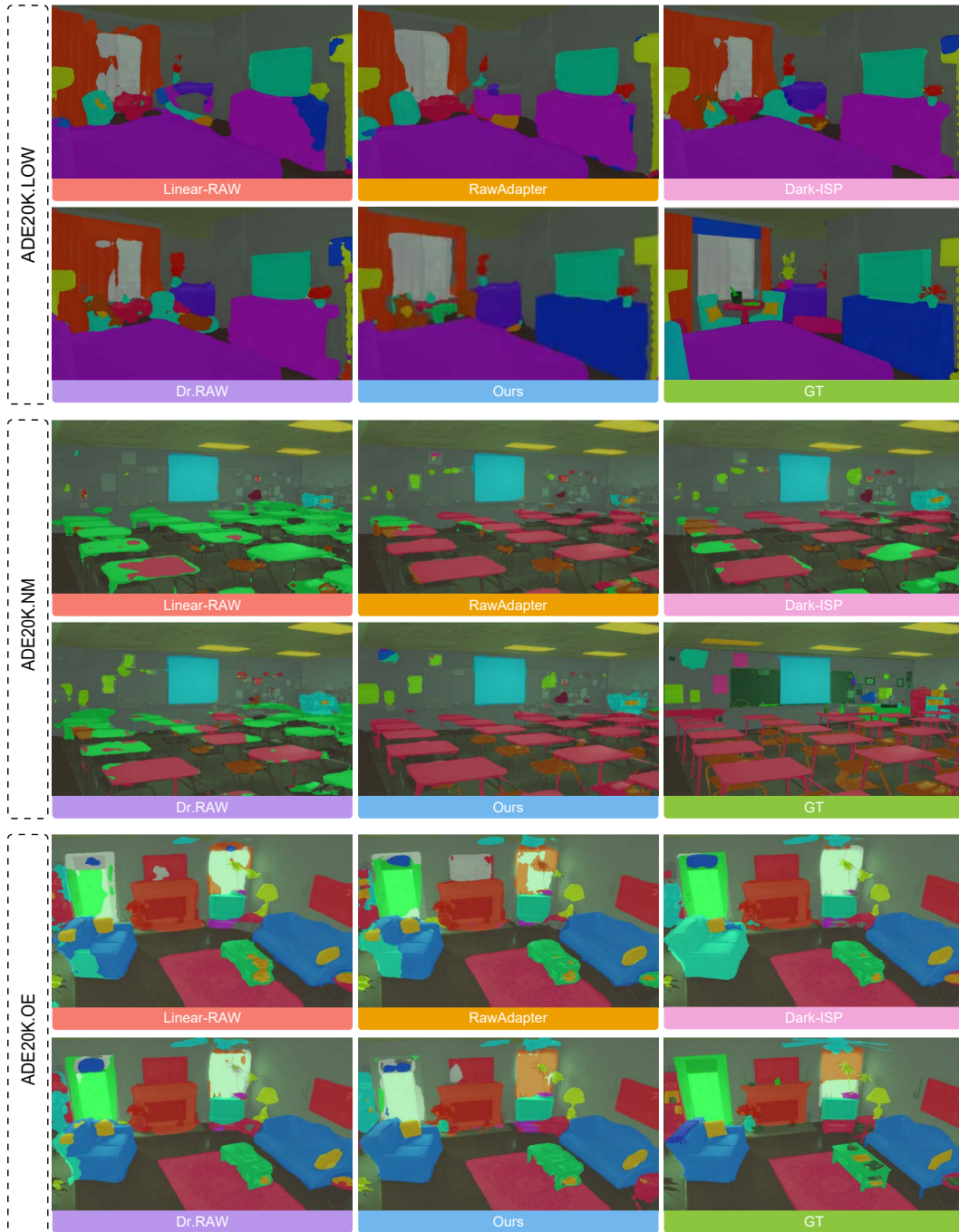


Figure 21: Qualitative transfer results on exposure-curated ADE20K under three illumination regimes: Low-light (*LOW*), Normal (*NM*), and Over-exposure (*OE*). Our method yields more coherent regions and cleaner semantic boundaries across all three settings.

References

- Mahmoud Afifi, Luxi Zhao, Abhijith Punnappurath, Mohamed A Abdelsalam, Ran Zhang, and Michael S Brown. Time-aware auto white balance in mobile photography. In *Proceedings of the IEEE/CVF International Conference on Computer Vision*, pages 5038–5047, 2025.
- Kobus Barnard, Lindsay Martin, Adam Coath, and Brian Funt. A comparison of computational color constancy algorithms. ii. experiments with image data. *IEEE Transactions on Image Processing*, 11(9):985–996, 2002.
- Chinmay Belthangady and Loic A Royer. Applications, promises, and pitfalls of deep learning for fluorescence image reconstruction. *Nature Methods*, 16(12):1215–1225, 2019.
- Radu Berdan, Beril Besbinar, Christoph Reinders, Junji Otsuka, and Daisuke Iso. Reraw: Rgb-to-raw image reconstruction via stratified sampling for efficient object detection on the edge. In *Proceedings of the IEEE/CVF Conference on Computer Vision and Pattern Recognition*, pages 11833–11843, 2025.
- Tim Brooks, Ben Mildenhall, Tianfan Xue, Jiawen Chen, Dillon Sharlet, and Jonathan T Barron. Unprocessing images for learned raw denoising. In *Proceedings of the IEEE/CVF Conference on Computer Vision and Pattern Recognition*, pages 11036–11045, 2019.
- Mark Buckler, Suren Jayasuriya, and Adrian Sampson. Reconfiguring the imaging pipeline for computer vision. In *Proceedings of the IEEE International Conference on Computer Vision*, pages 975–984, 2017.
- Gengjia Chang, Xining Ge, Weijun Yuan, Zhan Li, Qiorong Song, Luen Zhu, and Shuhong Liu. Beyond model design: Data-centric training and self-ensemble for gaussian color image denoising. *arXiv preprint arXiv:2604.11468*, 2026a.
- Gengjia Chang, Xining Ge, Weijun Yuan, Zhan Li, Qiorong Song, Luen Zhu, and Shuhong Liu. Training-free model ensemble for single-image super-resolution via strong-branch compensation. *arXiv preprint arXiv:2604.11564*, 2026b.
- Chen Chen, Qifeng Chen, Jia Xu, and Vladlen Koltun. Learning to see in the dark. In *Proceedings of the IEEE conference on Computer Vision and Pattern Recognition*, pages 3291–3300, 2018.
- Jiawen Chen, Sylvain Paris, and Frédo Durand. Real-time edge-aware image processing with the bilateral grid. *ACM Transactions on Graphics*, 26(3):103–es, 2007.
- Jiawen Chen, Andrew Adams, Neal Wadhwa, and Samuel W Hasinoff. Bilateral guided upsampling. *ACM Transactions on Graphics*, 35:1–8, 2016.
- Jiji Chen, Hideki Sasaki, Hoyin Lai, Yijun Su, Jiamin Liu, Yicong Wu, Alexander Zhovmer, Christian A Combs, Ivan Rey-Suarez, Hung-Yu Chang, et al. Three-dimensional residual channel attention networks denoise and sharpen fluorescence microscopy image volumes. *Nature Methods*, 18(6):678–687, 2021.
- Linwei Chen, Ying Fu, Kaixuan Wei, Dezhi Zheng, and Felix Heide. Instance segmentation in the dark. *International Journal of Computer Vision*, 131(8):2198–2218, 2023.
- CIE (International Commission on Illumination). Recommendations on uniform colour-spaces-colour difference equations, psychometric colour terms, 1978.
- Commission Internationale de l’Eclairage. Method of measuring and specifying colour rendering properties of light sources. Technical Report CIE 013.3-1995, CIE, 1995.
- Commission Internationale de l’Eclairage. Colorimetry. Technical Report CIE 015:2018, CIE, 2018.
- Marcos V Conde, Javier Vazquez-Corral, Michael S Brown, and Radu Timofte. Nilut: Conditional neural implicit 3d lookup tables for image enhancement. In *Proceedings of the AAAI Conference on Artificial Intelligence*, volume 38, pages 1371–1379, 2024.
- Ziteng Cui and Tatsuya Harada. Raw-adapter: Adapting pre-trained visual model to camera raw images. In *European Conference on Computer Vision*, pages 37–56. Springer, 2024.

- Ziteng Cui, Guo-Jun Qi, Lin Gu, Shaodi You, Zenghui Zhang, and Tatsuya Harada. Multitask aet with orthogonal tangent regularity for dark object detection. In *Proceedings of the IEEE/CVF International Conference on Computer Vision*, pages 2553–2562, 2021.
- Ziteng Cui, Jianfei Yang, and Tatsuya Harada. Raw-adapter: Adapting pre-trained visual model to camera raw images and a benchmark. *arXiv preprint arXiv:2503.17027*, 2025.
- Mauricio Delbracio, Damien Kelly, Michael S Brown, and Peyman Milanfar. Mobile computational photography: A tour. *Annual Review of Vision Science*, 7(1):571–604, 2021.
- Steven Diamond, Vincent Sitzmann, Frank Julca-Aguilar, Stephen Boyd, Gordon Wetzstein, and Felix Heide. Dirty pixels: Towards end-to-end image processing and perception. *ACM Transactions on Graphics*, 40(3):1–15, 2021.
- Graham D Finlayson. Corrected-moment illuminant estimation. In *Proceedings of the IEEE International Conference on Computer Vision*, pages 1904–1911, 2013.
- Shani Gamrian, Hila Barel, Feiran Li, Masakazu Yoshimura, and Daisuke Iso. Beyond rgb: Adaptive parallel processing for raw object detection. In *Proceedings of the IEEE/CVF International Conference on Computer Vision*, pages 5547–5557, 2025.
- Xining Ge, Gengjia Chang, Weijun Yuan, Zhan Li, Zhanglu Chen, Boyang Yao, Yihang Chen, Yifan Deng, and Shuhong Liu. Dual-branch remote sensing infrared image super-resolution. *arXiv preprint arXiv:2604.10112*, 2026a.
- Xining Ge, Weijun Yuan, Gengjia Chang, Xuyang Li, and Shuhong Liu. Clip-guided data augmentation for night-time image dehazing. *arXiv preprint arXiv:2604.05500*, 2026b.
- Michaël Gharbi, Gaurav Chaurasia, Sylvain Paris, and Frédo Durand. Deep joint demosaicking and denoising. *ACM Transactions on Graphics*, 35(6):1–12, 2016.
- Michaël Gharbi, Jiawen Chen, Jonathan T Barron, Samuel W Hasinoff, and Frédo Durand. Deep bilateral learning for real-time image enhancement. *ACM Transactions on Graphics*, 36(4):1–12, 2017.
- Jiasheng Guo, Xin Gao, Yuxiang Yan, Guanghao Li, and Jian Pu. Dark-isp: Enhancing raw image processing for low-light object detection. In *Proceedings of the IEEE/CVF International Conference on Computer Vision*, pages 9583–9593, 2025.
- Yuduo Guo, Hao Zhang, Mingyu Li, Fujiang Yu, Yunjing Wu, Yuhan Hao, Song Huang, Yongming Liang, Xiaojing Lin, Xinyang Li, et al. Deeper detection limits in astronomical imaging using self-supervised spatiotemporal denoising. *Science*, page eady9404, 2026.
- Khurram Azeem Hashmi, Goutham Kallempudi, Didier Stricker, and Muhammad Zeshan Afzal. Featenhancer: Enhancing hierarchical features for object detection and beyond under low-light vision. In *Proceedings of the IEEE/CVF International Conference on Computer Vision*, pages 6725–6735, 2023.
- Kaiming He, Xiangyu Zhang, Shaoqing Ren, and Jian Sun. Deep residual learning for image recognition. In *Proceedings of the IEEE/CVF Conference on Computer Vision and Pattern Recognition*, pages 770–778, 2016.
- Glenn E Healey and Raghava Kondepudy. Radiometric ccd camera calibration and noise estimation. *IEEE Transactions on Pattern Analysis and Machine Intelligence*, 16(3):267–276, 2002.
- Felix Heide, Markus Steinberger, Yun-Ta Tsai, Mushfiqur Rouf, Dawid Pająk, Dikpal Reddy, Orazio Gallo, Jing Liu, Wolfgang Heidrich, Karen Egiazarian, et al. Flexisp: A flexible camera image processing framework. *ACM Transactions on Graphics*, 33(6):1–13, 2014.
- Yashar D Hezaveh, Laurence Perreault Lévassieur, and Philip J Marshall. Fast automated analysis of strong gravitational lenses with convolutional neural networks. *Nature*, 548(7669):555–557, 2017.
- Mingbo Hong, Shen Cheng, Haibin Huang, Haoqiang Fan, and Shuaicheng Liu. You only look around: learning illumination-invariant feature for low-light object detection. *Advances in Neural Information Processing Systems*, 37:87136–87158, 2024.

- Yang Hong, Kaixuan Wei, Linwei Chen, and Ying Fu. Crafting object detection in very low light. In *The British Machine Vision Conference*, volume 1, page 3, 2021.
- Wenjun Huang, Ziteng Cui, Yinqiang Zheng, Yirui He, Tatsuya Harada, and Mohsen Imani. Dr. RAW: Towards general high-level vision from RAW with efficient task conditioning. In *Annual Conference on Neural Information Processing Systems*, 2025.
- Hai Jiang, Binhao Guan, Zhen Liu, Xiaohong Liu, Jian Yu, Zheng Liu, Songchen Han, and Shuaicheng Liu. Learning to see in the extremely dark. In *Proceedings of the IEEE/CVF International Conference on Computer Vision*, pages 7676–7685, 2025.
- Jun Jiang, Dengyu Liu, Jinwei Gu, and Sabine Süsstrunk. What is the space of spectral sensitivity functions for digital color cameras? In *IEEE Workshop on Applications of Computer Vision (WACV)*, pages 168–179. IEEE, 2013.
- Xin Jin, Pengyi Jiao, Zheng-Peng Duan, Xingchao Yang, Chongyi Li, Chun-Le Guo, and Bo Ren. Lighting every darkness with 3dgs: Fast training and real-time rendering for hdr view synthesis. *Advances in Neural Information Processing Systems*, 37:80191–80219, 2024.
- Hakki Can Karaimer and Michael S Brown. A software platform for manipulating the camera imaging pipeline. In *European Conference on Computer Vision*, pages 429–444. Springer, 2016.
- Eric Kee, Adam Pikielny, Kevin Blackburn-Matzen, and Marc Levoy. Removing reflections from raw photos. In *Proceedings of the Computer Vision and Pattern Recognition Conference*, pages 161–171, 2025.
- Wontae Kim and Nam Ik Cho. Image-adaptive 3d lookup tables for real-time image enhancement with bilateral grids. In *European Conference on Computer Vision*, pages 91–108. Springer, 2024.
- Woohyeok Kim, Geonu Kim, Junyong Lee, Seungyong Lee, Seung-Hwan Baek, and Sunghyun Cho. Paramisp: Learned forward and inverse isps using camera parameters. *arXiv preprint arXiv:2312.13313*, 2023.
- Hoang M Le, Brian Price, Scott Cohen, and Michael S Brown. Gamutmlp: a lightweight mlp for color loss recovery. In *Proceedings of the IEEE/CVF Conference on Computer Vision and Pattern Recognition*, pages 18268–18277, 2023.
- Gongzhe Li, Linwei Qiu, Peibei Cao, Fengying Xie, Xiangyang Ji, and Qilin Sun. Real-time scene-adaptive tone mapping for high-dynamic range object detection. In *Annual Conference on Neural Information Processing Systems*, 2025a.
- Ruikang Li, Yujin Wang, Shiqi Chen, Fan Zhang, Jinwei Gu, and Tianfan Xue. Dualdn: Dual-domain denoising via differentiable isp. In *European Conference on Computer Vision*, pages 160–177. Springer, 2024a.
- Zhihao Li, Ming Lu, Xu Zhang, Xin Feng, M Salman Asif, and Zhan Ma. Efficient visual computing with camera raw snapshots. *IEEE Transactions on Pattern Analysis and Machine Intelligence*, 46(7):4684–4701, 2024b.
- Zhihao Li, Yufei Wang, Alex Kot, and Bihan Wen. From chaos to clarity: 3dgs in the dark. *Advances in Neural Information Processing Systems*, 37:94971–94992, 2024c.
- Zhong-Yu Li, Xin Jin, Bo-Yuan Sun, Chun-Le Guo, and Ming-Ming Cheng. Towards raw object detection in diverse conditions. In *Proceedings of the IEEE/CVF Conference on Computer Vision and Pattern Recognition*, pages 8859–8868, 2025b.
- Panjun Liu, Jiacheng Li, Lizhi Wang, Zheng-Jun Zha, and Zhiwei Xiong. Mlp embedded inverse tone mapping. In *Proceedings of the 32nd ACM International Conference on Multimedia*, pages 1283–1291, 2024.
- Shuhong Liu, Chenyu Bao, Ziteng Cui, Yun Liu, Xuangeng Chu, Lin Gu, Marcos V Conde, Ryo Umagami, Tomohiro Hashimoto, Zijian Hu, et al. Realx3d: A physically-degraded 3d benchmark for multi-view visual restoration and reconstruction. *arXiv preprint arXiv:2512.23437*, 2025a.

- Shuhong Liu, Xiang Chen, Hongming Chen, Quanfeng Xu, and Mingrui Li. Deraings: Gaussian splatting for enhanced scene reconstruction in rainy environments. In *Proceedings of the AAAI Conference on Artificial Intelligence*, volume 39, pages 5558–5566, 2025b.
- Shuhong Liu, Tianchen Deng, Heng Zhou, Liuzhuozheng Li, Hongyu Wang, Danwei Wang, and Mingrui Li. Mg-slam: Structure gaussian splatting slam with manhattan world hypothesis. *IEEE Transactions on Automation Science and Engineering*, 2025c.
- Shuhong Liu, Lin Gu, Ziteng Cui, Xuangeng Chu, and Tatsuya Harada. I2-nerf: Learning neural radiance fields under physically-grounded media interactions. *arXiv preprint arXiv:2510.22161*, 2025d.
- Shuhong Liu, Chenyu Bao, Ziteng Cui, Xuangeng Chu, Bin Ren, Lin Gu, Xiang Chen, Mingrui Li, Long Ma, Marcos V Conde, et al. Ntire 2026 3d restoration and reconstruction in real-world adverse conditions: Realx3d challenge results. *arXiv preprint arXiv:2604.04135*, 2026a.
- Shuhong Liu, Xining Ge, Ziteng Cui, Liuzhuozheng Li, Gengjia Chang, Jun Liu, Ziyang Gu, Dong Li, Xuangeng Chu, Lin Gu, and Tatsuya Harada. Fluxflow: Conservative flow-matching for astronomical image super-resolution. *arXiv preprint arXiv:2605.03749*, 2026b.
- Shuhong Liu, Xining Ge, Ziyang Gu, Quanfeng Xu, Lin Gu, Ziteng Cui, Xuangeng Chu, Jun Liu, Dong Li, and Tatsuya Harada. Denoising the deep sky: physics-based ccd noise formation for astronomical imaging. *arXiv preprint arXiv:2601.23276*, 2026c.
- Tie Liu, Yuhui Quan, Yingna Su, Yang Guo, Shu Liu, Haisheng Ji, Qi Hao, Yulong Gao, Yuxia Liu, Yikang Wang, et al. Astronomical image denoising by self-supervised deep learning and restoration processes. *Nature Astronomy*, 9(4):608–615, 2025e.
- Ze Liu, Yutong Lin, Yue Cao, Han Hu, Yixuan Wei, Zheng Zhang, Stephen Lin, and Baining Guo. Swin transformer: Hierarchical vision transformer using shifted windows. In *Proceedings of the IEEE/CVF International Conference on Computer Vision*, pages 10012–10022, 2021.
- Calvin S McCamy, Harold Marcus, James G Davidson, et al. A color-rendition chart. *J. App. Photog. Eng*, 2(3):95–99, 1976.
- Ben Mildenhall, Peter Hedman, Ricardo Martin-Brualla, Pratul P Srinivasan, and Jonathan T Barron. Nerf in the dark: High dynamic range view synthesis from noisy raw images. In *Proceedings of the IEEE/CVF Conference on Computer Vision and Pattern Recognition*, pages 16190–16199, 2022.
- Seonghyeon Nam, Abhijith Punnappurath, Marcus A Brubaker, and Michael S Brown. Learning srgb-to-raw-rgb de-rendering with content-aware metadata. In *Proceedings of the IEEE/CVF Conference on Computer Vision and Pattern Recognition*, pages 17704–17713, 2022.
- Elias Nehme, Daniel Freedman, Racheli Gordon, Boris Ferdman, Lucien E Weiss, Onit Alalouf, Tal Naor, Reut Orange, Tomer Michaeli, and Yoav Shechtman. Deepstorm3d: dense 3d localization microscopy and psf design by deep learning. *Nature Methods*, 17(7):734–740, 2020.
- Alex Omid-Zohoor, Christopher Young, David Ta, and Boris Murmann. Toward always-on mobile object detection: Energy versus performance tradeoffs for embedded hog feature extraction. *IEEE Transactions on Circuits and Systems for Video Technology*, 28(5):1102–1115, 2017.
- Chawin Ounkomol, Sharmishta Seshamani, Mary M Maleckar, Forrest Collman, and Gregory R Johnson. Label-free prediction of three-dimensional fluorescence images from transmitted-light microscopy. *Nature Methods*, 15(11):917–920, 2018.
- Hao Ouyang, Zifan Shi, Chenyang Lei, Ka Lung Law, and Qifeng Chen. Neural camera simulators. In *Proceedings of the IEEE/CVF Conference on Computer Vision and Pattern Recognition*, pages 7700–7709, 2021.
- Wei Ouyang, Andrey Aristov, Mickaël Lelek, Xian Hao, and Christophe Zimmer. Deep learning massively accelerates super-resolution localization microscopy. *Nature Biotechnology*, 36(5): 460–468, 2018.

- Jin-Hwi Park, Chanhwi Jeong, Junoh Lee, and Hae-Gon Jeon. Depth prompting for sensor-agnostic depth estimation. In *Proceedings of the IEEE/CVF Conference on Computer Vision and Pattern Recognition*, pages 9859–9869, 2024.
- William Peebles and Saining Xie. Scalable diffusion models with transformers. In *Proceedings of the IEEE/CVF International Conference on Computer Vision*, pages 4195–4205, 2023.
- Georgy Perevozchikov, Nancy Mehta, Mahmoud Afifi, and Radu Timofte. Rawformer: Unpaired raw-to-raw translation for learnable camera ISPs. In *European Conference on Computer Vision*, pages 231–248. Springer, 2024.
- Max Planck. Über das gesetz der energieverteilung im normalspektrum. In *Von Kirchhoff bis Planck: Theorie der Wärmestrahlung in historisch-kritischer Darstellung*, pages 178–191. Springer, 1978.
- Irwin G Priest. A proposed scale for use in specifying the chromaticity of incandescent illuminants and various phases of daylight. *Journal of the Optical Society of America*, 23(2):41–45, 1933.
- Abhijith Punnappurath and Michael S Brown. Learning raw image reconstruction-aware deep image compressors. *IEEE Transactions on Pattern Analysis and Machine Intelligence*, 42(4):1013–1019, 2019.
- Abhijith Punnappurath and Michael S Brown. Spatially aware metadata for raw reconstruction. In *Proceedings of the IEEE/CVF Winter Conference on Applications of Computer Vision*, pages 218–226, 2021.
- Abhijith Punnappurath, Abdullah Abuolaim, Abdelrahman Abdelhamed, Alex Levinshtein, and Michael S Brown. Day-to-night image synthesis for training nighttime neural ISPs. In *Proceedings of the IEEE/CVF Conference on Computer Vision and Pattern Recognition*, pages 10769–10778, 2022.
- Chang Qiao, Di Li, Yuting Guo, Chong Liu, Tao Jiang, Qionghai Dai, and Dong Li. Evaluation and development of deep neural networks for image super-resolution in optical microscopy. *Nature Methods*, 18(2):194–202, 2021.
- Ilija Radosavovic, Raj Prateek Kosaraju, Ross Girshick, Kaiming He, and Piotr Dollár. Designing network design spaces. In *Proceedings of the IEEE/CVF Conference on Computer Vision and Pattern Recognition*, pages 10428–10436, 2020.
- Erik Reinhard, Wolfgang Heidrich, Paul Debevec, Sumanta Pattanaik, Greg Ward, and Karol Myszkowski. *High dynamic range imaging: acquisition, display, and image-based lighting*. Morgan Kaufmann, 2010.
- SanerYee. Deep understanding tesla FSD: Photon to control. Medium, December 2023. URL <https://saneryee-studio.medium.com/deep-understanding-tesla-fsd-photon-to-control-48577fab8070>.
- Yukihiro Sasagawa and Hajime Nagahara. Yolo in the dark-domain adaptation method for merging multiple models. In *European Conference on Computer Vision*, pages 345–359. Springer, 2020.
- David Serrano-Lozano, Luis Herranz, Michael S Brown, and Javier Vazquez-Corral. Namedcurves: Learned image enhancement via color naming. In *European Conference on Computer Vision*, pages 92–108. Springer, 2024.
- Artur Speiser, Lucas-Raphael Müller, Philipp Hoess, Ulf Matti, Christopher J Obara, Wesley R Legant, Anna Kreshuk, Jakob H Macke, Jonas Ries, and Srinivas C Turaga. Deep learning enables fast and dense single-molecule localization with high accuracy. *Nature Methods*, 18(9):1082–1090, 2021.
- Jiayu Sun, Ke Xu, Youwei Pang, Lihe Zhang, Huchuan Lu, Gerhard Hancke, and Rynson Lau. Adaptive illumination mapping for shadow detection in raw images. In *Proceedings of the IEEE/CVF International Conference on Computer Vision*, pages 12709–12718, 2023.
- Sabine Süsstrunk, Robert Buckley, and Steve Swen. Standard rgb color spaces. In *Color and Imaging Conference*, volume 7, pages 127–134. Society of Imaging Science and Technology, 1999.

- Ashish Vaswani, Noam Shazeer, Niki Parmar, Jakob Uszkoreit, Llion Jones, Aidan N Gomez, Łukasz Kaiser, and Illia Polosukhin. Attention is all you need. *Advances in Neural Information Processing Systems*, 30, 2017.
- Hongda Wang, Yair Rivenson, Yiyin Jin, Zhensong Wei, Ronald Gao, Harun Günaydın, Laurent A Bentolila, Comert Kural, and Aydogan Ozcan. Deep learning enables cross-modality super-resolution in fluorescence microscopy. *Nature Methods*, 16(1):103–110, 2019.
- Nan Wang, Yuantao Chen, Lixing Xiao, Weiqing Xiao, Bohan Li, Zhaoxi Chen, Chongjie Ye, Shaocong Xu, Saining Zhang, Ziyang Yan, et al. Unifying appearance codes and bilateral grids for driving scene gaussian splatting. *arXiv preprint arXiv:2506.05280*, 2025.
- Xinzhe Wang, Kang Ma, Qiankun Liu, Yunhao Zou, and Ying Fu. Multi-object tracking in the dark. In *Proceedings of the IEEE/CVF Conference on Computer Vision and Pattern Recognition*, pages 382–392, 2024a.
- Yuehao Wang, Chaoyi Wang, Bingchen Gong, and Tianfan Xue. Bilateral guided radiance field processing. *ACM Transactions on Graphics*, 43(4):1–13, 2024b.
- Yufei Wang, Yi Yu, Wenhan Yang, Lanqing Guo, Lap-Pui Chau, Alex C Kot, and Bihan Wen. Raw image reconstruction with learned compact metadata. In *Proceedings of the IEEE/CVF Conference on Computer Vision and Pattern Recognition*, pages 18206–18215, 2023.
- Yufei Wang, Yi Yu, Wenhan Yang, Lanqing Guo, Lap-Pui Chau, Alex C Kot, and Bihan Wen. Beyond learned metadata-based raw image reconstruction. *International Journal of Computer Vision*, 132(12):5514–5533, 2024c.
- Yujin Wang, Tianyi Xu, Fan Zhang, Tianfan Xue, and Jinwei Gu. Adaptiveisp: Learning an adaptive image signal processor for object detection. *Advances in Neural Information Processing Systems*, 37:112598–112623, 2024d.
- Kaixuan Wei, Ying Fu, Jiaolong Yang, and Hua Huang. A physics-based noise formation model for extreme low-light raw denoising. In *Proceedings of the IEEE/CVF Conference on Computer Vision and Pattern Recognition*, pages 2758–2767, 2020.
- Martin Weigert, Uwe Schmidt, Tobias Boothe, Andreas Müller, Alexandr Dibrov, Akanksha Jain, Benjamin Wilhelm, Deborah Schmidt, Coleman Broaddus, Siân Culley, et al. Content-aware image restoration: pushing the limits of fluorescence microscopy. *Nature Methods*, 15(12):1090–1097, 2018.
- Qi Wu, Janick Martinez Esturo, Ashkan Mirzaei, Nicolas Moenne-Loccoz, and Zan Gojcic. 3dgt: Enabling distorted cameras and secondary rays in gaussian splatting. *Proceedings of the IEEE/CVF Conference on Computer Vision and Pattern Recognition*, 2025.
- Günther Wyszecki and Walter Stanley Stiles. *Color science: concepts and methods, quantitative data and formulae*. John wiley & sons, 2000.
- Enze Xie, Wenhai Wang, Zhiding Yu, Anima Anandkumar, Jose M Alvarez, and Ping Luo. Segformer: Simple and efficient design for semantic segmentation with transformers. *Advances in Neural Information Processing Systems*, 34:12077–12090, 2021.
- Haiyang Xie, Xi Shen, Shihua Huang, Qirui Wang, and Zheng Wang. Simrod: A simple baseline for raw object detection with global and local enhancements. In *Proceedings of the AAAI Conference on Artificial Intelligence*, volume 40, pages 11051–11059, 2026.
- Yazhou Xing, Zian Qian, and Qifeng Chen. Invertible image signal processing. In *Proceedings of the IEEE/CVF Conference on Computer Vision and Pattern Recognition*, pages 6287–6296, 2021.
- Ruikang Xu, Chang Chen, Jingyang Peng, Cheng Li, Yibin Huang, Fenglong Song, Youliang Yan, and Zhiwei Xiong. Toward raw object detection: A new benchmark and a new model. In *Proceedings of the IEEE/CVF Conference on Computer Vision and Pattern Recognition*, pages 13384–13393, 2023.

- Masakazu Yoshimura, Junji Otsuka, Atsushi Irie, and Takeshi Ohashi. Dynamicisp: dynamically controlled image signal processor for image recognition. In *Proceedings of the IEEE/CVF International Conference on Computer Vision*, pages 12866–12876, 2023.
- Ke Yu, Zexian Li, Yue Peng, Chen Change Loy, and Jinwei Gu. Reconfigisp: Reconfigurable camera image processing pipeline. In *Proceedings of the IEEE International Conference on Computer Vision*, 2021.
- Syed Waqas Zamir, Aditya Arora, Salman Khan, Munawar Hayat, Fahad Shahbaz Khan, Ming-Hsuan Yang, and Ling Shao. Cycleisp: Real image restoration via improved data synthesis. In *Proceedings of the IEEE/CVF Conference on Computer Vision and Pattern Recognition*, pages 2696–2705, 2020.
- Vahid Zehtab, David B Lindell, Marcus A Brubaker, and Michael S Brown. Efficient neural network encoding for 3d color lookup tables. In *Proceedings of the AAAI Conference on Artificial Intelligence*, volume 39, pages 9772–9779, 2025.
- Chen Zhang, Wencheng Han, Yang Zhou, Jianbing Shen, Cheng-zhong Xu, and Wentao Liu. Leveraging frame affinity for srgb-to-raw video de-rendering. In *Proceedings of the IEEE/CVF Conference on Computer Vision and Pattern Recognition*, pages 25659–25668, 2024.
- Cheng Zhang, Boying Li, Meng Wei, Yan-Pei Cao, Camilo Cruz Gambardella, Dinh Phung, and Jianfei Cai. Unified camera positional encoding for controlled video generation. *arXiv preprint arXiv:2512.07237*, 2025.
- Yuxuan Zhang, Bo Dong, and Felix Heide. All you need is raw: Defending against adversarial attacks with camera image pipelines. In *European conference on computer vision*, pages 323–343. Springer, 2022.
- Chenhao Zheng, Ayush Shrivastava, and Andrew Owens. Exif as language: Learning cross-modal associations between images and camera metadata. In *Proceedings of the IEEE/CVF Conference on Computer Vision and Pattern Recognition*, pages 6945–6956, 2023.
- Bolei Zhou, Hang Zhao, Xavier Puig, Tete Xiao, Sanja Fidler, Adela Barriuso, and Antonio Torralba. Semantic understanding of scenes through the ade20k dataset. *International Journal of Computer Vision*, 127(3):302–321, 2019.